



National Library
of Canada

Acquisitions and
Bibliographic Services Branch

395 Wellington Street
Ottawa, Ontario
K1A 0N4

Bibliothèque nationale
du Canada

Direction des acquisitions et
des services bibliographiques

395, rue Wellington
Ottawa (Ontario)
K1A 0N4

Your file / Votre référence

Our file / Notre référence

NOTICE

The quality of this microform is heavily dependent upon the quality of the original thesis submitted for microfilming. Every effort has been made to ensure the highest quality of reproduction possible.

If pages are missing, contact the university which granted the degree.

Some pages may have indistinct print especially if the original pages were typed with a poor typewriter ribbon or if the university sent us an inferior photocopy.

Reproduction in full or in part of this microform is governed by the Canadian Copyright Act, R.S.C. 1970, c. C-30, and subsequent amendments.

AVIS

La qualité de cette microforme dépend grandement de la qualité de la thèse soumise au microfilmage. Nous avons tout fait pour assurer une qualité supérieure de reproduction.

S'il manque des pages, veuillez communiquer avec l'université qui a conféré le grade.

La qualité d'impression de certaines pages peut laisser à désirer, surtout si les pages originales ont été dactylographiées à l'aide d'un ruban usé ou si l'université nous a fait parvenir une photocopie de qualité inférieure.

La reproduction, même partielle, de cette microforme est soumise à la Loi canadienne sur le droit d'auteur, SRC 1970, c. C-30, et ses amendements subséquents.

**A Numerical Study of the Mesoscale Environment in a Case
of Severe Convective outbreak over Alberta**

By

Cunqiang Li

A dissertation submitted to the Faculty of Graduate Studies & Research in partial
fulfilment of requirements for the degree of
Master of Science

Department of Atmospheric and Oceanic Sciences
McGill University
Montreal, Quebec
CANADA

March, 1996



National Library
of Canada

Acquisitions and
Bibliographic Services Branch

395 Wellington Street
Ottawa, Ontario
K1A 0N4

Bibliothèque nationale
du Canada

Direction des acquisitions et
des services bibliographiques

395, rue Wellington
Ottawa (Ontario)
K1A 0N4

Your file *Votre référence*

Our file *Notre référence*

The author has granted an irrevocable non-exclusive licence allowing the National Library of Canada to reproduce, loan, distribute or sell copies of his/her thesis by any means and in any form or format, making this thesis available to interested persons.

L'auteur a accordé une licence irrévocable et non exclusive permettant à la Bibliothèque nationale du Canada de reproduire, prêter, distribuer ou vendre des copies de sa thèse de quelque manière et sous quelque forme que ce soit pour mettre des exemplaires de cette thèse à la disposition des personnes intéressées.

The author retains ownership of the copyright in his/her thesis. Neither the thesis nor substantial extracts from it may be printed or otherwise reproduced without his/her permission.

L'auteur conserve la propriété du droit d'auteur qui protège sa thèse. Ni la thèse ni des extraits substantiels de celle-ci ne doivent être imprimés ou autrement reproduits sans son autorisation.

ISBN 0-612-12226-3

Canada

Résumé

Dans cette étude, on examine l'environnement synoptique et mésoéchelle d'un cas de développement sévère de convection en Alberta les 11-12 juillet 1985 à l'aide du modèle Mésoéchelle Compressible Communautaire (MC2). Les résultats de l'expérience de contrôle confirment le modèle conceptuel et la conclusion de Smith et Yau (1993a,b). Une série d'expériences de sensibilité a été menée afin d'étudier les effets de l'évapotranspiration à la surface, la topographie, le réchauffement dû au rayonnement de courtes longueurs d'ondes et le refroidissement dû au rayonnement de grandes longueurs d'ondes. Les résultats des expériences de sensibilité démontrent 1) qu'augmentant la résolution horizontale des modèles mésoéchelles va probablement préciser davantage le moment et l'endroit du développement sévère de convection, mais la prévision mésoéchelle ne sera pas améliorée en simplement réduisant la taille de la grille. Un traitement réaliste de la topographie, des processus de surface et la physique des modèles est essentiel dans la prévision du développement sévère de convection. 2) que l'évapotranspiration locale à la surface est une importante source d'humidité. Sans l'évapotranspiration à la surface, trop peu d'humidité est transportée au bas des Rocheuses pour nourrir la convection. Le résultat est que la circulation montagne-plaine n'est plus assez efficace dans l'initiation de la convection sévère. 3) qu'une condition souvent observée pour la convection sévère, la présence d'une forte inversion de température, est formée suite à deux processus. Un facteur est la présence de refroidissement dû aux ondes longues à la surface. Un autre facteur est l'advection qui descend la pente des montagnes et le réchauffement adiabatique qui l'accompagne. Un fort réchauffement à la surface est essentiel à l'érosion de l'inversion de température au bas des montagnes.

ABSTRACT

In this study, the synoptic and mesoscale environment of a case of severe convective outbreak over Alberta on 11-12 July 1985 are investigated using the state-of-the-art Mesoscale Compressible Community Model (MC2). The results of the control experiment confirm the conceptual model and the conclusion of Smith and Yau (1993a,b). A series of sensitivity experiments were conducted to study the effects of surface evapotranspiration, topography, shortwave heating and longwave cooling. The results of the sensitivity experiments are 1) While increasing horizontal resolution of mesoscale models will likely improve the timing and location of the severe convective outbreak, the improvement in mesoscale forecast cannot be achieved by simply reducing the grid size. Realistic treatment of topography, surface processes, and model physics are essential to predict severe convective outbreak. 2) Local surface evapotranspiration was shown to be an important source of moisture. Without surface evapotranspiration, not enough moisture is transported to the foothills to feed the convection. As a result, the mountain-plain circulation became ineffective in initiating severe convection. 3) An often observed condition for severe convection, the presence of a strong capping lid, was found to be formed from two processes. One factor is the presence of radiative cooling at the surface. Another factor is the advection from the downslope flow and the accompanying diabatic warming. Strong surface heating is essential in eroding the lid over the foothills.

Table of Contents

RESUME	i
ABSTRACT	ii
Table of Contents	iii
List of Figures	v
List of Tables	ix
Acknowledgments	x
Chapter 1 Introduction	1
1.1 Background	1
1.2 Objectives of the thesis	3
Chapter 2 Model description	6
2.1 Dynamic equations	6
2.2 Model physics	10
a) Kuo cumulus parameterization	10
b) Sundqvist scheme	13
c) Explicit microphysics scheme	13
d) Terminal velocity adjustment	16
e) Planetary Boundary Layer and other parameterizations	18
2.3 Initialization of the model	21
2.4 List of experiments	22
Chapter 3 Control experiments	29
3.1 Comparison with satellite and radar observation	29
3.2 Comparison with observed synoptic-scale environment	31
3.3 Mesoscale analyses	33
a) Weakening of capping lid by surface heating	33

b) Underrunning and low-level moisture transport	34
c) Cross section of anomalous fields	34
 Chapter 4 Sensitivity Experiments	 48
4.1 Expt. NGE-Surface evapotranspiration turned off	48
4.2 Expts. LRT and FLAT-Reduced topographic forcing	50
4.3 Expts. NLW and NSW-reducing radiative forcing	51
 Chapter 5 Conclusions	 62
5.1 Summary and conclusions	62
5.2 Suggestions for future research	63
 REFERENCES	 65

List of Figures

Fig. 1.1	Schematic diagram of synoptic-scale features present on days of severe convective outbreaks. Long-dash line indicates axis of 500-mb height and thermal troughs. Dash-dot line indicates axis of 500-mb height and thermal ridges. Thin connected arrows show core of maximum 500-mb winds. Short-dash line is surface moisture tongue. Thick arrow is surface synoptic flow. The area of maximum destabilization is located over the foothills where maximum upper-level cooling is superimposed over maximum surface heating.	5
Fig. 1.2	Schematic vertical cross section for 08-14 LDT illustrating the amplified mountain-plain circulation and underrunning of the capping lid.	5
Fig. 2.1	The nested-domain of the MC2 model used in this study. A, B, C, and D boxes indicate the 100 km, 50 km, 25 km, and 10 km grid size portion of the domain, respectively.	26
Fig. 2.2	Topography for experiment CON in the 10km grid size. Contour interval is 250m.	27
Fig. 2.3	Topography for experiment LRT in the 10km grid size. Contour interval is 250m.	28
Fig. 3.1	Infrared satellite image of Alberta taken from a NOAA polar-orbiting satellite at 12UTC (06 LDT) 11 July 1985.	36
Fig. 3.2	Model predicted relative humidity field at 600mb at a) 06 LDT(12 UTC), b) 14 LDT(20 UTC), and c) 16 LDT(22 UTC) from 10 km control run. Contours are 70%,80%, 90%, and 95%. Shaded areas are relative humidity higher than 95%.	37
Fig. 3.3	Radar PPIs for a) 16LDT,11 July (22 UTC,11 July), b) 18LDT,11 July (24 UTC,11 July), and c) 20LDT,11 July(02 UTC, 12 July) with mesoscale analysis domain included. Range markers are spaced 20km apart. Contours are of radar reflectivity with an interval of 10 dB. Minimum contour is 20 dBZ. Elevation angle is 1.8°. The weak ground echoes near 240°, at a range of 120 - 140 km, are from the higher peaks in	

the Alberta foothills. 38

Fig. 3.4 Model predicted radar reflectivity field at 600mb at a) 16 LDT, 11 July 1985 (22UTC, 11 July 1985), b) 18 LDT, 11 July 1985 (00UTC, 12 July 1985), and c) 20 LDT, 11 July 1985 (02UTC, 12 July 1985) from 10 km control run. Contour interval every 10 dBZ. Minimum contour is 20 dBZ. The dashed circle denotes the 120 km range marker centred at Red Deer. 39

Fig. 3.5 Forecast at 500mb valid at a) Model initial time (18 LDT, 10 July 1985), b) 06 LDT (12 UTC), c) 12 LDT (18 UTC), and d) 18 LDT (24 UTC), 11 July 1985 from 100 km control run. Height (solid), 500-1000mb thickness (dashed) contours are in decameters. 40

Fig. 3.6 CMC 500mb analysis at a) 18 LDT, 10 July 1985 (00 UTC, 11 July 1985), b) 06 LDT (12 UTC), c) 12 LDT (18 UTC), and d) 18 LDT (24 UTC), 11 July 1985 from 100 km control run. Height (solid), 500-1000mb thickness (dashed) contours are in decameters. 41

Fig. 3.7 Model predicted MSL pressure and surface wind at a) 08 LDT (14 UTC), b) 12 LDT (18 UTC), and c) 18 LDT (24 UTC), 11 July 1985 from 10 km resolution control run. Contour interval is 2 mb. The largest wind vector is 8m/s. 42

Fig. 3.8 Forecast 10 km resolution surface dew point temperature at a) 08 LDT (14 UTC), b) 12 LDT (18 UTC), and c) 18 LDT (24 UTC), 11 July 1985. Contour interval every 2°C. 43

Fig. 3.9 Vertical cross-section of temperature at a) 00 LDT (06 UTC), b) 08 LDT (14 UTC), and c) 10 LDT (16 UTC), 11 July 1985 from 10 km resolution control run. The location of the section is indicated by the line from 1 to 2 in Fig. 2.1. Contour interval is 1°C. The largest wind vector is 13m/s. 44

Fig. 3.10 Vertical cross-section of a) air temperature and b) dew point temperature at 14 LDT (20 UTC), 11 July 1985 from 10 km resolution control run. The location of the section is indicated by the line from 1 to 2 in Fig. 2.1. Contour interval is 1°C. The largest wind vector is 13m/s. 45

Fig. 3.11	Forecast horizontal section of anomalous mean sea level pressure at a) 08 LDT (14 UTC), b) 12 LDT (18 UTC), and c) 18 LDT (24 UTC) from 25 km resolution run. The contour interval is 0.5 mb.	46
Fig. 3.12	Forecast vertical cross sections of anomalous equivalent potential temperature at a) 12LDT, and b) 16 LDT and anomalous u-component of the wind at c) 12LDT and d) 16 LDT on 11 July 1985 from 10 km resolution run. The contour intervals for temperature and wind are 1°K and 1 ms ⁻¹ respectively. The location of vertical cross section is the same as in Fig. 4 in SY93a.	47
Fig. 4.1	Forecast surface dew point temperature without surface evapotranspiration at a) 08 LDT (14 UTC), b) 12 LDT (18 UTC), and c) 18 LDT (24 UTC), 11 July 1985 from 10 km run. Contour interval is 2°C.	53
Fig. 4.2	Vertical cross-section of specific humidity difference between Expt. CON. and Expt. NGE at a) 00 LDT (06 UTC), b) 08 LDT (14 UTC), c) 10 LDT (16 UTC), and d) 16 LDT (22 UTC), 11 July 1985. The contour interval is 1 g kg ⁻¹ . The location of the section is indicated by the line from 1 to 2 in Fig. 2.1.	54
Fig. 4.3	Forecast MSL pressure for Expt. LRT at a) 08 LDT (14 UTC), b) 12 LDT (18 UTC), and c) 18 LDT (24 UTC), 11 July 1985 from 10 km run. The contour interval is 2 mb.	55
Fig. 4.4	Forecast MSL pressure for Expt. FLAT at a) 08 LDT (14 UTC), b) 12 LDT (18 UTC), and c) 18 LDT (24 UTC), 11 July 1985 from 10 km run. The contour interval is 2 mb.	56
Fig. 4.5	Forecast surface dew point temperature for Expt. LRT at a) 08 LDT (14 UTC), b) 12 LDT (18 UTC), and c) 18 LDT (24 UTC), 11 July 1985 from 10 km run. The contour interval is 2°C.	57
Fig. 4.6	Vertical cross-section of U component of the wind difference between Expt. CON and Expt. LRT at a) 08 LDT (14 UTC), b) 12 LDT (18 UTC), and c) 16 LDT (22 UTC), 11 July 1985. The contour interval is 1 ms ⁻¹ . The location of the section is indicated by the line from 1 to 2 in Fig. 2.1.	58

Fig. 4.7	Vertical cross-section of specific humidity difference between Expt. CON and Expt FLAT at a) 08 LDT (14 UTC), b) 10 LDT (16 UTC), c) 12 LDT (18 UTC), and d) 14 LDT (20 UTC), 11 July 1985. The contour interval is 0.5 gkg ⁻¹ . The location of the section is indicated by the line from 1 to 2 in Fig. 2.1.	59
Fig. 4.8	Vertical cross-section of temperature in Expt NLW at a) 00 LDT (06 UTC), b) 02 LDT (08 UTC), c) 04 LDT (10 UTC), and d) 06 LDT (12 UTC), 11 July 1985. The contour interval is 1°C. The largest wind vector is 13ms ⁻¹ . The location of the section is indicated by the line from 1 to 2 in Fig. 2.1.	60
Fig. 4.9	Vertical cross-section of temperature in Expt NSW at a) 06 LDT (12 UTC), b) 08 LDT (14 UTC), c) 12 LDT (18 UTC), and d) 18 LDT (24 UTC), 11 July 1985. The contour interval is 1°C. The largest wind vector is 13ms ⁻¹ . The location of the section is indicated by the line from 1 to 2 in Fig. 2.1.	61

List of Tables

Table 2.1 Summary of MC2.	23
Table 2.2 Summary of the nested-grid model.	24
Table 2.3 49 Gal-Chen levels.	25

Acknowledgements

First and foremost, I sincerely thank my supervisor, Prof. M.K.(Peter) Yau, for his uninterrupted devotion and patience during the course of this research. I benefited greatly from his high scientific standard, keen physical insights and constructive criticisms, and his mastery of mesoscale modelling and dynamics. I am very grateful to Dr. Robert Benoit for his persistent and patient help and stimulating discussions during this research. I gratefully acknowledge the support of the MC2 model group at the Recherche en Prevision Numerique (RPN) of the Atmospheric Environment Service of Canada (AES). I would like to acknowledge the aid of Mr. Alan Schwartz in solving numerous software and hardware problems over the years. I also acknowledge financial support from CIDA (Canada International Development Agency), McGill University, and research support from Prof. Yau. I like to thank them for providing me with this opportunity for advancing my knowledge in meteorology. I am indebted to my friends in this department for their aid during the long and difficult months spent in this study. I thank Dr. Fanyau Kong, Mr. Zonghui Huo, and Mr. Bao Ning for their stimulating discussions . Finally, I want to thank my family for their patience, support, and love without which the completion of this dissertation would not have been possible.

Chapter 1

Introduction

1.1 Background

According to Smith and Yau (1993a, hereafter SY93a) "central Alberta is a region highly susceptible to severe summertime convection. Climatological statistics show that the area is affected by hail on an average of 61 days each summer (Wojtiw 1975) and between 10 to 20 tornadoes are reported annually (Bullas and Wallace 1988; see also Newark 1984). Although most of the hail comes from relatively weak single and multicell storms, highly organized multi or supercell storms develop three to five times a summer and produce widespread, large hail and/or tornadoes."

They remarked that "on days with severe convection in central Alberta, the morning soundings generally show a low-level tropospheric inversion or capping lid which initially inhibits the formation of deep convection. Towering cumulus clouds first form over the foothills region in the early afternoon. Under suitable conditions, they intensify rapidly into cumulonimbus which move eastward."

To investigate the essential synoptic-physical processes that distinguish severe convective events, Smith and Yau (1993a, 1993b, hereafter SY93b) carried out a detailed analysis of a high resolution data set collected in a mesoscale experiment over Alberta (Limestone Mountain EXperiment 1985 - LIMEX-85). In particular, they compared a severe

convective event which occurred on 11 July 1985 with other case days with lesser or little convection. Their primary conclusions are:

- 1) Under generally clear sky conditions, cumulus convection begins over the Alberta foothills, where the capping lid is quickly eroded by strong surface heating.
- 2) Most severe convective outbreaks appear to occur when cooling aloft, associated with an approaching synoptic-scale, upper-level trough is in phase with strong surface heating over the foothills. The surface synoptic pressure gradient provides for east-northeasterly winds over the plains which transport moist plains air towards the foothills and into the lower-branch of the mountain-plain circulation. Such a configuration brings about localized, deep destabilization which gives rise to strong upslope moisture transport.
- 3) The mountain-plain circulation is ineffective in initiating severe convection when subsidence warming associated with an upstream ridge inhibits its growth, and surface synoptic pressure gradient provides for northwesterly, westerly or southwesterly winds over the plains. Under these conditions, the plains moisture is advected away from the foothills, so that by the time the thermally-induced upslope flow has developed, its moisture content has been depleted to the point of being unable to support severe convection.

From the results of the analysis of 11 LIMEX-85 case days, SY93b proposed a conceptual model of the outbreak of severe convection over Alberta. Their model is summarized in Figs. 1.1 and 1.2. In short, the model proposed that most severe convective events result when upper-level cooling, associated with an advancing, synoptic-scale trough, occurs in phase with strong surface heating over the Alberta foothills. The deep destabilization over the elevated topography acts to amplify the mountain-plain circulation

and to generate mesoscale upslope moisture transport. Concurrently, the surface synoptic pressure gradient gives rise to east-northeasterly winds which advect the moisture-rich air of the eastern plains into the lower-branch of the mountain-plain circulation. In this manner, the plains moisture is permitted to reach the convectively active foothills through underrunning of the capping lid. The end product is the initiation of well-organized, severe convective storms which move eastward with the westerly component of the mid-tropospheric winds.

Because of the limitation of the dataset, there were several outstanding questions left unanswered. One of which is what is the principle moisture source for convection in Alberta? Does it come from a tongue of modified maritime tropical air which enters the Prairie provinces in southern Manitoba and extends westward into east-central Alberta, or does an important fraction of the low-level moisture originate from evapotranspiration? Another question is what causes the formation of the capping lid in Alberta? Could the lid be the result of a subsidence inversion enhanced locally near the foothills by orography or does the lid arise partly due to advection of an elevated mixed layer (Carlson et al. 1983) into central Alberta. There is also evidence in the LIMEX-85 data that lid formation in Alberta may be partly the result of radiative cooling at the surface. What are the relative contribution of all these factors?

1.2 Objective of the thesis

The purpose of this thesis is to validate the conceptual model of SY93b by numerical simulation using the state-of-the-art Mesoscale Compressible Community mesoscale model (MC2) (Tanguay et al. 1990) and to carry out sensitivity experiments to shed light on the

importance of various physical processes. Specifically, we will simulate the mesoscale environment of a case of severe convective outbreak over Alberta. This case occurred on 11 to 12 July 1985 during LIMEX-85 and was analyzed extensively in SY93a. The main tasks are:

- 1). to carry out a 30 h simulation of the 11 July 1985 case and compare the results with the analysis given in SY93a,
- 2). to investigate the importance of topography, surface evapotranspiration, and long and short wave radiation, and
- 3). to determine the principal moisture source for severe convection over the foothills of Alberta.

The organization of the thesis is as follows: Chapter 2 summarizes the main features of the model and the initial conditions. Chapter 3 presents a comparison of the simulation and observational analysis for the case day. Chapter 4 contains results of sensitivity tests. Summary and conclusions are in Chapter 5.

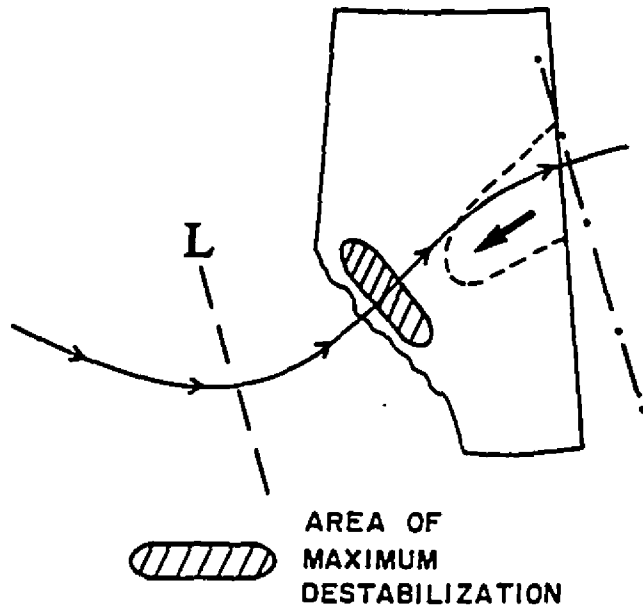


Fig. 1.1 Schematic diagram of synoptic-scale features present on days of severe convective outbreaks. Long-dash line indicates axis of 500-mb height and thermal troughs. Dash-dot line indicates axis of 500-mb height and thermal ridges. Thin connected arrows show core of maximum 500-mb winds. Short-dash line is surface moisture tongue. Thick arrow is surface synoptic flow. The area of maximum destabilization is located over the foothills where maximum upper-level cooling is superimposed over maximum surface heating.

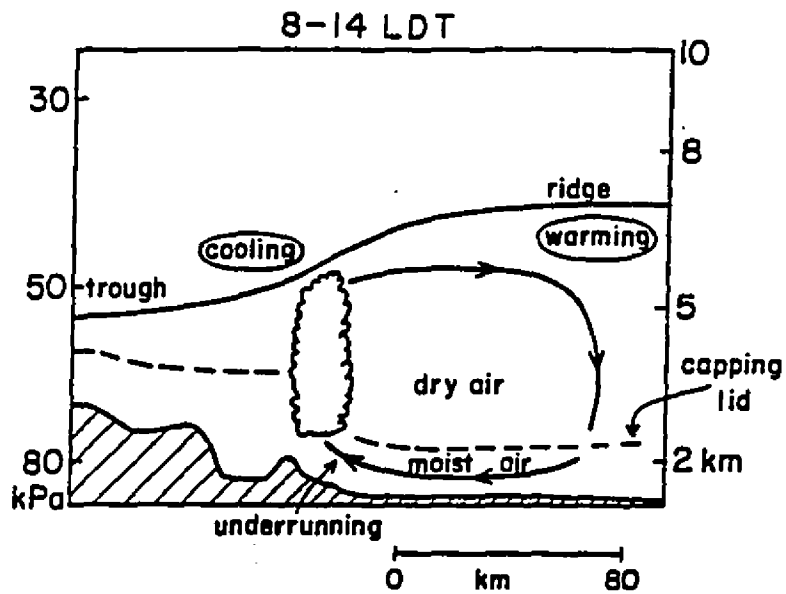


Fig. 1.2 Schematic vertical cross section for 08-14 LDT illustrating the amplified mountain-plain circulation and underrunning of the capping lid.

Chapter 2

Model Description

The basic numerical model is version 3.2 of MC2. It has been modified to include explicit equations for cloud water and rain water contents. The main features are summarized in Table 2.1. A one-way nesting strategy is employed and the nested domains are depicted in Fig.2.1. Terrain data for domains A ($\Delta X=100\text{km}$), B ($\Delta X=50\text{km}$), and C ($\Delta X=25\text{km}$) are obtained from topographical tapes at RPN (Division de la recherche en prevision numerique), a laboratory of the Atmospheric Environment Service (AES) at Dorval. Terrain data for the D($\Delta X=10\text{km}$) domain are from the U.S. Navy database. We describe the model dynamics in section 2.1, and the model physics in section 2.2. The initialization of the model will be discussed in section 2.3.

2.1 Dynamic Equations

To describe atmospheric motion the Euler equations are first transformed from a local Cartesian coordinate (x, y) to a transformed coordinate (X, Y) with a conformal projection:

$$\begin{pmatrix} dX \\ dY \end{pmatrix} = \begin{bmatrix} -\sin\lambda & -\cos\lambda \\ \cos\lambda & -\sin\lambda \end{bmatrix} \begin{pmatrix} dx \\ dy \end{pmatrix} \quad (1)$$

where λ is the longitude. Following a well-known procedure, we define a terrain-following vertical coordinate Z where the lowest level is coincident with the ground. This vertical coordinate simplifies the treatment of lower boundary conditions and allows more efficient use of computer resources. The following functional form for Z is adopted (Gal-Chen and Somerville 1975)

$$Z = \left(\frac{z - h_0}{H - h_0} \right) H \quad (2)$$

where h_0 is the height of topography. H is the top of the model atmosphere.

Within this framework the field equations become:

$$\frac{dU}{dt} - fV - K \frac{\partial S}{\partial X} - RT \left(\frac{\partial q}{\partial X} + \frac{G_1}{G_0} \frac{\partial q}{\partial Z} \right) + F_X \quad (3)$$

$$\frac{dV}{dt} + fU - K \frac{\partial S}{\partial Y} - RT \left(\frac{\partial q}{\partial Y} + \frac{G_2}{G_0} \frac{\partial q}{\partial Z} \right) + F_Y \quad (4)$$

$$\frac{dw}{dt} + \frac{-RT}{G_0} \frac{\partial q}{\partial Z} - g + F_Z \quad (5)$$

$$(1 - \alpha) \frac{dq}{dt} = -S \left(\frac{G_1 U + G_2 V}{G_0 (H - Z)} \right) - S \left(\frac{\partial U}{\partial X} + \frac{\partial V}{\partial Y} \right) - \frac{\partial W}{\partial Z} + \frac{Q}{T} \quad (6)$$

$$\frac{dT}{dt} = \alpha T \frac{dq}{dt} + Q \quad (7)$$

$$\frac{dq_v}{dt} = E \quad (8)$$

$$\frac{dq_c}{dt} = S_c \quad (9)$$

$$\frac{dq_r}{dt} = S_R \quad (10)$$

where

$$q = \ln p \quad (11)$$

$$G_0 = \frac{H - h_0}{H} \quad (12)$$

$$G_1 = - \left(\frac{H - Z}{H} \right) \frac{\partial h_0}{\partial X} \quad (13)$$

$$G_2 = - \left(\frac{H - Z}{H} \right) \frac{\partial h_0}{\partial Y} \quad (14)$$

$$W = \frac{S(G_1 U + G_2) + w}{G_0} \quad (15)$$

$$S = \frac{U^2 + V^2}{2} \quad (16)$$

$$K = m^2 \cdot \left(\frac{1 + \sin \phi_0}{1 + \sin \phi} \right) \quad (17)$$

Here m is the map scale factor for a polar stereographic projection, $\alpha = R/C_p$ and Q is the diabatic term. (F_x, F_y, F_z) are the sources and/or sinks of momentum. The symbols q_v , q_c , and q_r are the mixing ratios for water vapour, cloud water, and rain water respectively and their corresponding source/sink terms are denoted by E , S_c , and S_R . All other symbols have their usual meanings.

With the above definitions, the scaled wind images (U,V) can be written in terms of the local Cartesian wind components (u,v) as

$$\begin{pmatrix} U \\ V \end{pmatrix} = \frac{1}{m} \begin{bmatrix} -\sin \lambda & -\cos \lambda \\ \cos \lambda & -\sin \lambda \end{bmatrix} \begin{pmatrix} u \\ v \end{pmatrix} \quad (18)$$

and the total derivative must be interpreted as:

$$\frac{d}{dt} = \frac{\partial}{\partial t} + S(U \frac{\partial}{\partial X} + V \frac{\partial}{\partial Y}) + W \frac{\partial}{\partial Z} \quad (19)$$

2.2 Model Physics

For the convective and microphysical processes, the model allows use of the Kuo cumulus parameterization, the Sundqvist scheme, and the explicit warm rain scheme.

a) Kuo cumulus parameterization

The parameterization is a modified form of the original version proposed by Kuo (1974) and is described in Mailhot et al. (1989). Cumulus convection is assumed to occur in a layer which is conditionally unstable and subject to a net convergence of moisture. The layer is marked by pressure surfaces p_1 and p_c . Cloudy parcels originates at p_1 , generally assumed to be the bottom level at the surface. As the parcels ascend, they will first be cooled dry adiabatically until the lifting condensation level p_b . Thereafter, the parcels rise moist adiabatically but with their temperature modified by the entrainment parameter λ . The level p_1 is the level of neutral buoyancy.

The net moisture convergence (Q_{AC}) is

$$Q_{AC} = -\frac{1}{g} \int_{p_t}^{p_t} \nabla \cdot (Vq_v) dp + E_0 \quad (20)$$

where the first term on the right represents the large-scale convergence of moisture and E_0 denotes surface evaporation. The moisture is assumed to be processed by the convective clouds. A fraction b is expended in moistening the environment and the remaining $(1-b)$ fraction condenses and precipitates out. Latent heat is released during the condensation process. Following Anthes (1977), the partition parameter b is prescribed to vary with the mean saturation deficit in the cloud layer:

$$b = \left[\frac{1 - \frac{1}{p_b - p_t} \int_{p_t}^{p_b} RH dp}{1 - RH_c} \right]^n \quad (21)$$

where RH and RH_c are the relative humidity and the critical relative humidity respectively. The values for n and RH_c are respectively 3 and 0.37. Because the moisture fraction expended in moistening the environment may subsequently precipitate out, the parameter b can be considered as a partition parameter between convective and non-convective

precipitation.

To calculate the vapour mixing ratio at a new time step, the equation $dq_v/dt = 0$ is first solved to obtain an intermediate value q_v^* . When convection does not occur, q_v at the new time step equals q_v^* . However when convection occurs, we compute the humidification Δq_v , defined as the product between the quantity bQ_{AC} and the ratio between the local environmental saturation deficit and the mean vapour deficit in the convectively active layer, as

$$\Delta q_v = \frac{bQ_{AC} [q_{vs}(T_c) - q_{ve}]}{p_b} \frac{1}{p_b - p_t} \int_{p_r} [q_{vs}(T_c) - q_{ve}] dp \quad (22)$$

where q_{vs} and q_{ve} are respectively the saturated water vapour mixing ratio and the vapour mixing ratio of the environment. We then add Δq_v to the value of q_v at the $(n-1)^{th}$ time step to arrive at the value for q_v at the $(n+1)^{th}$ time step. It is readily seen by vertically integrating the quantity Δq_v that the total effect of the clouds is to redistribute vertically the non-precipitating fraction (b) of the net moisture convergence Q_{AC} . The computational procedure outlined above would ensure that the moisture balance is maintained.

Condensation releases latent heat. The amount of latent heat released, $L(1-b)Q_{AC}$, is distributed vertically as a function of the difference between the virtue temperature of the cloud (T_{vc}) and that of the environment (T_{ve}). The change of temperature ΔT in a layer is therefore

$$\Delta T = \frac{L_v}{C_p} \frac{(1 - b) Q_{AC} (T_{vc} - T_w)}{p_b - p_t} \int_{p_t}^{p_b} (T_{vc} - T_w) dp \quad (23)$$

Note that this heating accounts only for the net condensation/evaporation term in the heat budget and does not account for the vertical heat transport by convection.

b) Sundqvist scheme

Sundqvist (1978) and Sundqvist et al (1989) developed a scheme to treat nonconvective condensation and precipitation. The scheme is developed for a grid size of 50 km for a meso- α model. Its basic assumption is that on such a grid size, condensation can be considered a subgrid-scale process and clouds can form in a grid box before the whole grid box reaches a relative humidity of 100%. We can therefore define in a grid volume a fractional area β within which clouds can form when the volume averaged relative humidity exceeds a specified critical value. Another simplification can be made by virtue of the fact that the time scale for fallout of precipitation is much shorter than the time resolution of a meso- α model so that precipitation particles can be assumed to fall out instantaneously. Thus no explicit equations for precipitation particles are required and only one equation governing the distribution of cloud water content needs to be solved. We will apply the scheme for a grid size ≥ 25 km.

c) Explicit Microphysics Scheme

When the grid resolution becomes finer, explicit predictive equations for precipitation

particles are required. Kong and Yau (1995) implemented a version of the microphysical parameterization of Kong (1991), and Kong et al. (1990; 1991) into MC2. The parameterization represents an extension of the work of Orville and Kopp (1977), and Cotton and Stephens (1982). At the time of writing, the hail and graupel categories have not been implemented. Thus for our high resolution simulations (grid size of 10 km), we only activate the "warm rain" version of the microphysical parameterization.

The major microphysical processes in the "warm rain" parameterization include (in SI units):

(1) Condensation of supersaturated vapour to form cloud water (VD_{vc})

$$VD_{vc} = \max (X , - q_c) \frac{1}{2\Delta t} \quad (24)$$

where X is the capacity for condensation/evaporation given by

$$X = -\Delta q_v = \frac{q_v^* - q_{vs}^*}{1 + \frac{4098.17 q_{vs}^* L_v}{C_p(T - 35.86)^2}} \quad (25)$$

here q_v^* is the intermediate value for q_v after advection. For a new time step,

$$q_v = q_v^* + \Delta q_v \quad (26)$$

(2) Auto-conversion of cloud water to rain water (CN_{cr})

$$CN_{cr} = 10^{-3} \max \{ (q_c - 0.5 \times 10^{-3}) , 0 \} \quad (27)$$

(3) Accretion of cloud water by rain drops (CL_{cr})

Assuming continuous accretion with collection efficiency E_{rc} , the expression is

$$CL_{cr} = \frac{\pi}{4} q_c \int_0^{\infty} E_{rc} D^2 v_r(D) N(D) dD \quad (28)$$

where the size distribution for rain drops is

$$N(D) = N_0 \exp(-\lambda D) \quad (29)$$

$$\lambda = \left(\frac{\pi \rho L N_0}{\rho q_r} \right)^{\frac{1}{4}} \quad (30)$$

with $N_0 = 10^7 \text{ m}^{-4}$ and

The terminal velocity for rain drops has the form

$$v_r(D) = 2.13 \left(\frac{g \rho L}{2 \rho} \right)^{1/2} D^{1/2} = 149.1 \left(\frac{D}{\rho} \right)^{1/2} \quad (31)$$

For $E_{rc} = 0.9$, the accretion term becomes

$$CL_{cr} = 2.2 \rho^{0.375} q_c q_r^{0.875} \quad (32)$$

For the vertical advection of rain water content, the mass-weighted mean terminal velocity is used. It is computed from

$$V_r = \frac{\int_0^{\infty} v_r(D) \Omega(D) dD}{\int_0^{\infty} D \Omega(D) dD} = 14.08 \rho^{-0.375} q_r^{0.125} \quad (33)$$

where $\Omega(D)$ is the mass of a rain drop with diameter D .

(4) Evaporation of rain drops in subsaturated air (VD_{ev})

The rate of evaporation is written as

$$VD_{ev} = \max [\min [-(X \cdot q_e), \min (q_r, 2 \Delta t E_p)], 0] \frac{1}{2 \Delta t} \quad (34)$$

where E_p is the evaporation capacity of rain drops with the form

$$E_p = \frac{1}{\rho} \int_0^{\infty} \left(\frac{dm}{dt} \right)_E N(D) dD \quad (35)$$

Here $(dm/dt)_E$ denotes the evaporation rate for a single rain drop and is given by

$$\left(\frac{dm}{dt} \right)_E = \frac{2\pi D \left(1 - \frac{q_v}{q_{vs}} \right) f(D)}{\frac{L_v}{KT} \left(\frac{L_v}{R_w T} - 1 \right) + \frac{R_w T}{D_f e_s(T)}} \quad (36)$$

f is the ventilation factor, $f(D) = 1 + 0.23 [v_r(D) D / \nu]^{1/2}$, ν is the kinematic viscosity coefficient,

K and D_f are the thermal conductivity of air and the diffusivity of water vapour, respectively,

L_v and R_w are the latent heat of vaporization and the air constant for vapour, respectively.

By substituting (36) into (35) and using (29) and (30) the expression for E_p becomes

$$E_p = \frac{1}{\rho} \left(1 - \frac{q_v}{q_{vs}} \right) \frac{A_r (\rho q_r)^{0.525}}{2.03 \times 10^4 \frac{1.54 \times 10^5}{e_s(T)}} \quad (37)$$

where

$$A_r = 1.6 \cdot 30.39 (\rho q_r)^{0.2046} \quad (38)$$

d) Terminal velocity adjustment

Precipitation particles moves relative to the ground with a velocity $(w-V)$, where V is the terminal fall speed of the precipitation particles. For rain drops, (33) shows that V is a weak function of rain water mixing ratio and it typically has a value of several ms^{-1} even for a small amount of rain water content. On the other hand, the magnitude of the vertical velocity w , can vary strongly with the grid size. In a mesoscale model with a grid size ≥ 25 km, the grid volume averaged w can be much smaller than the updraft in the convective core. However, the mass weighted fall speed is still quite large because of the weak dependence on rain water content. Thus the magnitude of $(w-V)$ in convective cores can be larger than in real situations and the precipitation particles can fall too fast relative to the ground. To avoid this situation in convective situations, we adjusted the terminal velocities according to the horizontal grid size. Specifically, the terminal fall speed V is replaced by αV where α varies with the horizontal resolution as

$$\alpha = 1, \text{ for } \Delta l < \Delta l_0; \quad (39)$$

and

$$\alpha = \frac{\Delta l}{\Delta l_0}, \text{ for } \Delta l_0 \leq \Delta l \leq \Delta l_1.$$

where

$$\Delta l = (\Delta x \Delta y)^{\frac{1}{2}} \quad (40)$$

For our work, we choose $\Delta l_0 = 2.5$ km, and $\Delta l_1 = 25$ km.

e) Planetary Boundary Layer (PBL) and Other Parameterizations

The PBL parameterization was originally developed by Mailhot and Benoit (1982) and Benoit et al (1989) and is modified by Delage (1988a, 1988b) and Mailhot (1992). In this scheme, the surface temperature and moisture are obtained differently over the ocean and over the continent.

Over the ocean, the surface temperature T_s is given by the climatological or analyzed sea surface temperature. It is held constant during an integration. The surface water vapour mixing ratio q_s is the saturation vapour mixing ratio at the temperature T_s .

Over the continent (including ice-covered ocean), the relevant moisture variable is the soil moisture fraction W_s (volume of water per unit volume of soil). It is predicted with the surface temperature using the "force-restore" method (Deardorff 1978; Benoit et al. 1989)

as

$$\frac{\partial T_s}{\partial t} = \frac{-2\sqrt{\pi}}{C_s \Delta} [H_s + L_v E_s + e_s(\alpha_{SB} T_s^4 - F_{ls}^-) - (1 - \alpha_s) F_{ss}^-] - \frac{2\pi}{\tau} (T_s - T_p)$$

where the surface sensible heat flux H_s and surface vapour flux E_s are given by

$$H_s = \rho c_p \left(\frac{T}{\theta} \right) \overline{w \theta'}_s \quad (42)$$

$$E_s = \rho \overline{w q'}_s \quad (43)$$

and

$$\frac{\partial W_s}{\partial t} = \frac{-C_1}{\rho_L d_1} (E_s - R) - \frac{C_2}{\tau} (W_s - W_p) \quad (44)$$

Here L_v is the latent heat of vaporization, σ_{SB} the Stefan-Boltzmann constant, ϵ_s the surface emissivity, α_s the surface albedo, C_s the heat capacity of the soil, Δ the depth of soil thermal diffusion diurnal wave given by $\Delta = (k_s \tau)^{1/2}$ with k_s being the soil thermal diffusivity and τ the period of rotation of the Earth. The symbols F_{ik} and F_{ss} denote the incoming infrared flux and the solar flux arriving at the surface respectively. The other variables T_p , R , d_1 and W_p are respectively the deep soil temperature, the precipitation rate, the thickness of the skin moisture layer, and the deep soil moisture fraction. C_1 and C_2 are dimensionless empirical coefficients.

During the integration, T_p is kept constant but the deep soil moisture fraction W_p is calculated from

$$\frac{\partial W_p}{\partial t} = \frac{1}{\rho_L d_2} (E_s - R) \quad (45)$$

where d_2 is a thickness whose magnitude is quite a bit larger than d_1 .

The soil moisture fraction W_s is used as a soil moisture availability factor in the calculating of evaporation using the Budyko-bucket method or the semi-potential approach and yields the following relation for the moisture content at the ground

$$q_s = q_a \cdot \min(1, W_s / W_k) (q_{vs}(T_s) - q_a) \quad (46)$$

where q_s is the water vapour specific humidity at the ground, q_a is the specific humidity of the air at the lowest grid point, and W_k is a threshold for potential evaporation ($W_k < W_{max}$).

With the surface temperature (T_s) and moisture (q_s) known, the corresponding surface fluxes can be obtained using the Monin-Obukhov similarity theory for the surface layer. The surface layer is a thin turbulent region above the surface where the vertical fluxes are quasi-constant with height.

Once the surface-layer fluxes are known, the tendencies due to turbulent vertical diffusion are calculated as follows:

$$\frac{\partial \psi}{\partial t} = \frac{1}{\rho} \frac{\partial}{\partial z} \left[\rho K_{\psi} \left(\frac{\partial \psi}{\partial z} - \gamma_{\psi} \right) \right] \quad (47)$$

where ψ represents u , v , q or θ . The vertical diffusion coefficients K_{ψ} varies with the intensity of the turbulent exchanges. The parameter γ_{ψ} denotes a counter-gradient term.

The boundary conditions for (47) are vanishing fluxes at the model top:

$$K_{\psi} \left(\frac{\partial \psi}{\partial z} - \gamma_{\psi} \right) = 0 \quad (48)$$

and continuity of the turbulent fluxes with surface-layer fluxes at the surface.

The vertical diffusion coefficient K_{ψ} is expressed as

$$K_{\psi} = \frac{c \lambda \sqrt{E}}{\phi_{\psi}} \quad (49)$$

where E is the turbulent kinetic energy (TKE), c is a constant (=.516), λ is a mixing length for the statically neutral case, and ϕ_w are stability functions determined locally by the Richardson number Ri . The details of the calculation are presented in Mailhot and Benoit (1982), Benoit et al (1989), Delage (1988a, 1988b) and Mailhot (1992).

2.3 Initialization of the model

To simulate the synoptic and mesoscale circulations which are important for the present problem, we used the strategy of grid nesting. Runs are conducted with 100 km, 50 km, 25 km, and 10 km resolutions with the coarser resolution runs furnishing initial and lateral boundary conditions to the finer resolution runs. The initial analysis for the 100 km run is taken from the CMC (Canadian Meteorological Centre) analysis. For the 100 km and 50 km runs, the Kuo cumulus parameterization and Sundqvist stable condensation scheme were used. For the 25 km and 10 km runs, the explicit "warm rain" microphysical scheme was employed. All runs were made with a vertical resolution of 49 levels, the detail vertical grid structure is given in Table 2.3. The simulations were initiated at 00 UTC 11 July 1985(18LDT 10 July 1985) and run for 30 hours. The time steps used for the 100 km, 50 km, 25 km, and 10 km runs are 10 min, 5 min, 1 min, and 30 s respectively. The so-called dynamic initialization technique (DIT) was used to adjust the mass and the flow fields at the initial time towards a balanced state in all runs. The summary of the properties for the nested-grid model is listed in Table 2.2.

2.4 List of experiments

The following experiments were performed.

<u>Experiment</u>	<u>Comments</u>
CON	Control experiment with parameters as in section 2.3
NGE	Surface evapotranspiration turned off over land
LRT	Lower resolution topography at 200 km resolution
FLAT	Flat topography
NLW	Longwave radiation turned off
NSW	Shortwave radiation turned off

Experiment CON will be described in Chapter 3. The other sensitivity experiments will be summarized in Chapter 4. The topographies for experiments CON and LRT in the 10 km grid are given respectively in Fig. 2.2 and Fig. 2.3.

TABLE 2.1 Summary of MC2

Dynamics

- * Non-hydrostatic primitive equations, u , v , T , p , q_v , q_c , and q_r predictive
- * Data in nesting sponge zone updated from prescribed lateral boundary conditions.
- * Semi-implicit time discretion
- * Staggered grid a polar-stereographic projection
- * 49 Gal-Chen levels with top at $H=15$ km
- * Second-order horizontal diffusion
- * 3-D semi-Lagrangian advection

Physics

- * Anthes/Kuo type convective parameterization
- * Turbulent Kinetic Energy (TKE) PBL treatment
- * Explicit warm rain microphysics
- * Surface fluxes computed from similarity theory
- * Implicit vertical diffusion
- * Prediction of ground temperature and moisture following the force-restore "slab" model

TABLE 2.2 Summary of the nested-grid model

domain properties	A	B	C	D
Grid increments	100km	50km	25km	10km
Moist physics	Kuo scheme plus Sundqvist scheme	Kuo scheme plus Sundqvist scheme	Explicit warm rain scheme	Explicit warm rain scheme
Grid dimensions	91x 71x49	111x101x49	131x111x49	151x141x49
Terrain data resolution	200km	100km	50km	20km
Time increments	600s	300s	60s	30s

TABLE 2.3 49 Gal-Chen Levels

Z_T	ΔZ_T	Z_M	ΔZ_M
0.0	-	9.4	9.4
18.8	18.8	28.3	18.9
37.8	19.0	47.3	19.0
56.8	19.0	66.3	19.0
75.9	19.1	85.5	19.2
95.1	19.2	104.8	19.3
114.4	19.3	124.1	19.3
133.8	19.4	143.6	19.5
153.3	19.5	165.1	21.5
176.9	23.6	190.7	25.6
204.5	27.6	220.5	29.8
236.4	31.9	254.5	34.0
272.6	36.2	292.9	38.4
313.2	40.6	335.8	42.9
358.4	45.2	383.3	47.5
408.3	49.9	435.7	52.4
463.1	54.8	493.1	57.4
523.1	60.0	555.7	62.6
588.4	65.3	623.9	68.2
659.4	71.0	697.8	73.9
736.3	76.9	777.8	80.0
819.4	83.1	864.3	86.5
909.2	89.8	957.7	93.4
1006.2	97.0	1058.5	100.8
1110.7	104.5	1167.1	108.6
1223.5	112.8	1284.3	117.2
1345.1	121.6	1410.7	126.4
1476.3	131.2	1547.2	136.5
1618.0	141.7	1694.7	147.5
1771.4	153.4	1854.5	159.8
1937.5	166.1	2027.8	173.3
2118.0	180.5	2216.2	188.4
2314.5	196.5	2425.5	209.3
2536.5	222.0	2658.5	233.0
2780.4	243.9	2915.0	256.5
3049.7	269.3	3199.3	284.3
3348.9	299.2	3516.5	317.2
3684.1	335.2	3873.6	357.1
4063.2	379.1	4280.2	406.6
4497.3	434.1	4749.8	469.6
5002.4	505.1	5302.6	552.8
5602.8	600.4	5970.4	667.8
6338.0	735.2	6861.5	891.1
7384.9	1046.9	8016.8	1155.3
8648.7	1263.8	9299.6	1282.8
9950.5	1301.8	10673.7	1374.1
11397.0	1446.5	12192.6	1518.9
12988.2	1591.3	13749.7	1557.1
14511.2	1523.0	14755.6	1005.9

Note: Z_T is the height of thermodynamic Gal-Chen Level
 Z_M is the height of momentum Gal-Chen Level

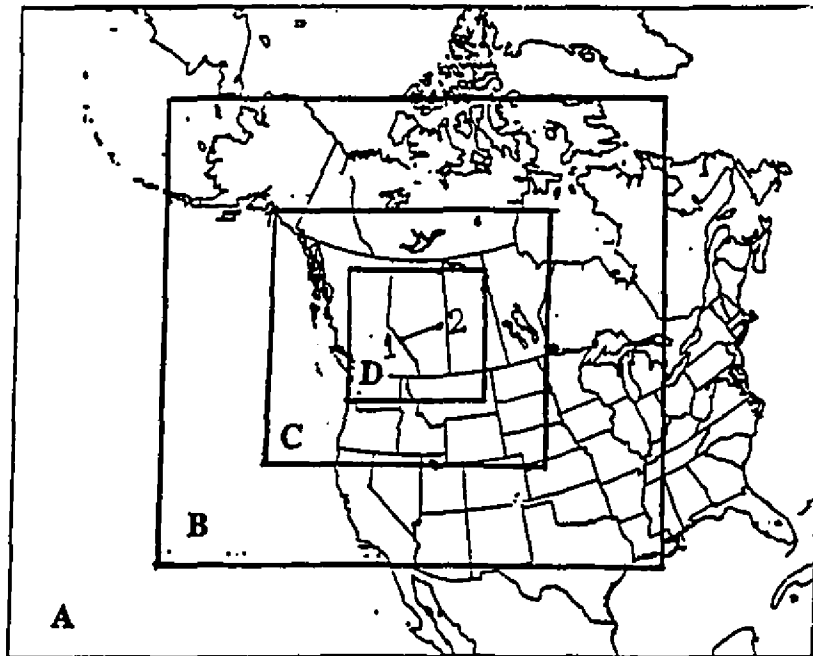


Fig. 2.1 The nested-domain of the MC2 model used in this study. A, B, C, and D boxes indicate the 100 km, 50 km, 25 km, and 10 km grid size portion of the domain, respectively.

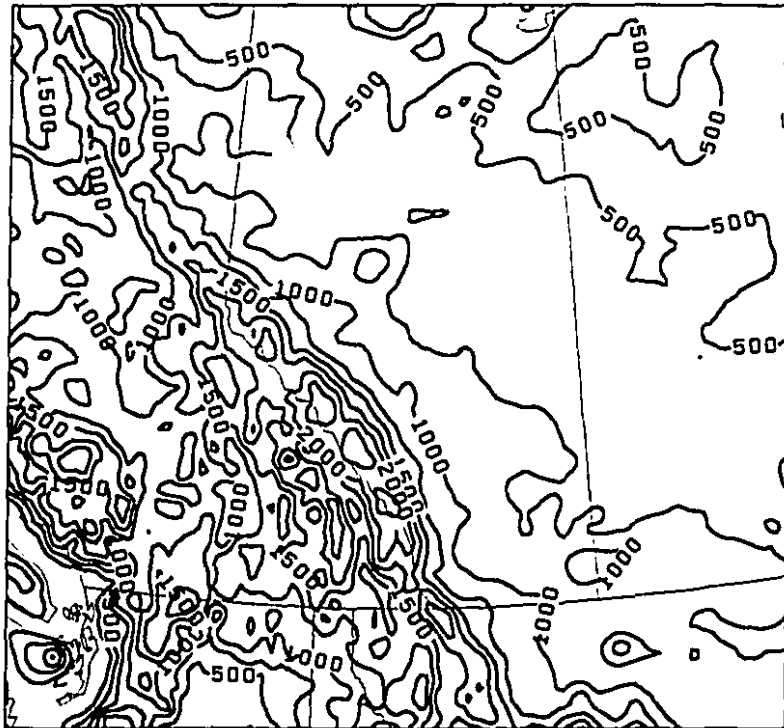


Fig. 2.2 Topography for experiment CON in the 10km grid size. Contour interval is 250m.

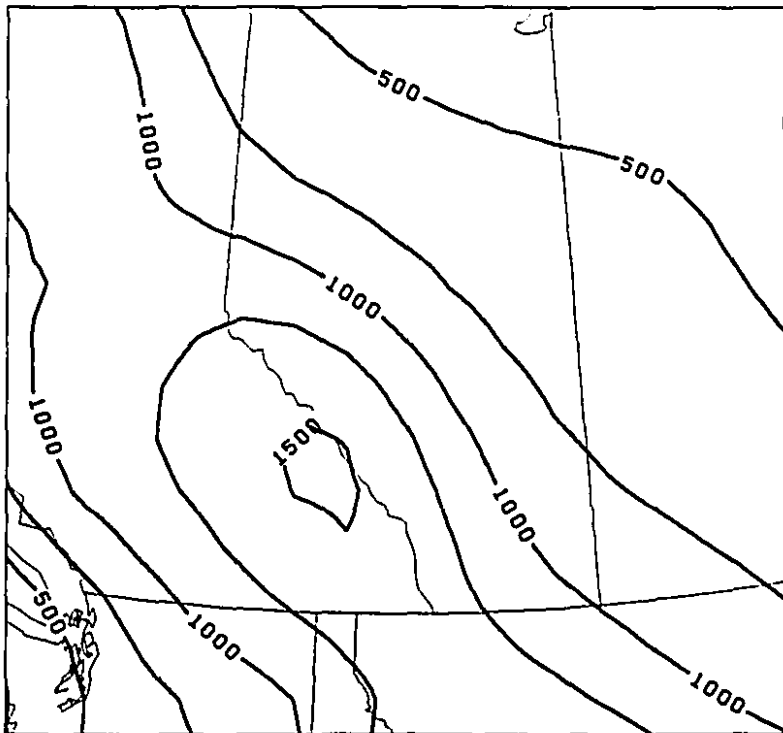


Fig. 2.3 Topography for experiment LRT in the 10km grid size. Contour interval is 250m.

Chapter 3

Control Experiment

This chapter presents the results for a 30 h control run for the July 11, 1985 LIMEX case. In section 3.1, we will compare the model output with satellite and radar observations. Comparison of the synoptic scale environment will be described in section 3.2 . Section 3.3 contains a comparison of the mesoscale features.

3.1 Comparison with satellite and radar observations

According to SY93a, this day was marked by well-organized multicell storms which began moving out of the foothills around 16 LDT(22 UTC). Radar reflectivities between 60 and 70 dBZ were presented in these storms over the course of several hours. A total of 228 hail reports were received and eight of these were for hail of golfball size (3.3 - 5.2 cm).

To compare the time evolution of the storm from observations and the control run, we show first the satellite imagery at 12 UTC (06 LDT) 11 July in Fig. 3.1. At this time, clear sky conditions prevailed over the foothills of Alberta while cloudy conditions were depicted over the northern half of the province. In agreement with satellite observations, the model predicted relative humidity at 600 mb at 12 UTC (06 LDT) (Fig. 3.2a, 12 h after the initial time) showed high values over the northern half of Alberta. The relative humidity over the southern half of the province was less than 70 %. A line of TCu started to form along the

foothills around 1534 LDT(2134 UTC), as depicted in an infrared satellite image presented in Figure 11 of SY93a. Similarly, the simulated 600 mb relative humidity indicated the presence of a cloud band near the same location from 14 LDT (20 UTC) to 16 LDT (22 UTC) (Figs 3.2b,c).

A sequence of radar observations from 16 LDT (22 UTC) to 20 LDT(02 UTC 12 July 1985) taken by the Alberta Research Council radar located at Red Deer is reproduced in Fig. 3.3. At 16 LDT (22 UTC) (Fig. 3.3a) , the first radar echo appeared at 300° at a range of 160 km. Two hours later, a large cell, with its maximum reflectivities reaching 60 dBz, can be found southwest of Edmonton (Fig. 3.3b). The storm continued to propagate eastward and two large echoes can be clearly identified at 20 LDT (02 UTC 12 July 1985) (Fig.3.3c).

The model generated radar reflectivities at the same times are depicted in Fig. 3.4. The reflectivities are computed from the rain water content at 600 mb which is roughly at the same height as the observed echoes on the 1.8° PPI at a range of 120 km. The Z-R relation used is

$$Z = 10 \log_{10} 200R^{1.6} \quad (dBZ)$$

where Z is the radar reflectivity in dBz and R is the rainfall rate in mm hr⁻¹.

The rainfall rate is computed from the rainwater content and the adjusted terminal fall velocity as

$$R = 3600 \rho_L V_r' q_r \quad (mm h^{-1})$$

At 16 LDT, two simulated small cells appeared at the western edge of the radar range

(Figure 3.4a). Two hours later, two large echoes were located southwest of Edmonton and their maximum reflectivities were reaching 50 dBz (Fig.3.4b). By 20 LDT (Fig. 3.4c) the storms have propagated to the south of Edmonton with their maximum reflectivities exceeding 50 dBz. A comparison of Fig. 3.3 and Fig. 3.4 indicated good agreement between the observation and the model results. The basic configuration and the locations of the echoes were well simulated. The propagation speed and the radar reflectivities were however smaller in the simulated storm. The latter aspect is attributable to the fact that only "warm rain" microphysics were included.

3.2 Comparison with observed synopticscale environment

SY93a,b pointed out the passage of an upstream 500 mb trough and the associated jet streak. Fig. 3.5 depicts the simulated 500 mb geopotential height, 500 mb wind vectors, and the 1000-500 mb thickness contours at 06, 12, and 18 LDT on 11 July. The corresponding CMC analyses are shown in Figure 3.6. For the most part, the model captured the major features in the 500 mb fields. The axes of the upper-level ridge and upper-level trough, situated at 00 UTC (18 LDT 10 July 1985) along the foothills of the Alberta and the eastern Pacific respectively (Fig. 3.5a), propagated eastward with time. By 1800 UTC (12 LDT), the axis of the ridge is over the Alberta-Saskatchewan border and the trough was just off the coast of British Columbia. The presence of the 500 mb trough upstream of central Alberta and a ridge downstream indicated favourable condition for large-scale ascent over the Alberta foothills.

In general, the location and amplitude of the model predicted upper-level wave (500 mb trough and ridge) were similar to the CMC objective analyses. However, the values of

the geopotential heights were larger by 10 to 15 m. The vector winds indicated the presence of an upper-level jet streak with speeds of 25 ms^{-1} at 500 mb and 38 ms^{-1} at 300 mb extending from south central British Columbia through central Alberta on into western Manitoba at 24 LDT (06 UTC 12 July 1985 LDT). The model-predicted the correct location of the jet streak but the wind speeds are smaller by 3 to 4 ms^{-1} . At 500 mb, net cooling occurred over central Alberta from 00 UTC to 24 UTC, 11 July (18 LDT, 10 July to 18 LDT, 11 July). This cooling was associated with the passage of the upper-level trough and was evident from the southeastward displacement with time of the 558 dm 1000 - 500 mb thickness contour in Fig. 3.6. This cooling trend was also produced in the model but the cooling rates were slightly too large.

The passage of the upper-level trough is often accompanied by the formation of lee-cyclones over the southern part of Alberta and Saskatchewan. Longley and Thompson (1965) and Strong (1986) suggested that an easterly component of the upslope flow, capable of the triggering severe convection, could be generated in the foothills by a baroclinic surface cyclone in southern Alberta. Similarly, a surface anticyclone located, for example, to the north of Edmonton, could yield the same effect.

Fig. 3.7 displays the model-predicted mean sea level pressure at 14 UTC (08 LDT), 18 UTC (12 LDT) and 24 UTC (18 LDT). At 14 UTC (Fig. 3.7a) a low pressure centre was situated over southeastern Alberta and a high pressure region can be found to the northwest of the LIMEX area. Although the winds were weak with a downslope component, the synoptic pressure gradient resulting from the high-low doublet favoured the formation of a northeasterly flow over the plain. The surface dew point temperature field (Figure 3.8a) was

distinguished by a tongue of moist air (follow for example the 12 °C line) extending from east central Alberta towards the northwest. Comparing Figs. 3.7a and 3.8a with the subjective analysis in SY93a (their Fig. 6) showed qualitative agreement of the pressure patterns. However, the model generated pressure values were higher by 2 to 4 mb. On the other hand, the tongue of moist air was quite well simulated in the model.

At 18 UTC (12 LDT), the simulated high pressure area (Figure 3.7b) extended southeastward and the low continued to deepen with a low trough extending towards the northwest. In the surface dew point temperature patterns (Figure 3.8b), the 12°C and 14°C isolines advanced southwestward to the northern part of the LIMEX area. The advancement of the dew point curves was consistent with the synoptic scale flow which was beginning to transport the moist air from the plains to the foothill region along the northern edge of the LIMEX experimental domain.

Six hours later (24 UTC), the southeastern low deepened to 1010 mb (Fig. 3.7c). A well-defined moisture tongue is shown to extend from the Alberta-Saskatchewan border up to the foothills northwest of the LIMEX area. The most intense multicell storms were formed in the foothills and moved eastward along the axis of this moisture ridge where dew point temperature exceeded 12 °C.

3.3 Mesoscale Features

a. Weakening of capping lid by surface heating

Fig. 3.9 shows the vertical cross-section of the temperature from 00 LDT to 10 LDT (06 UTC to 16 UTC). Over the plains, the inversion formed mainly during the night time

when there was strong cooling by long-wave radiation from the surface. Over the foothills, however, strong downslope flow developed and created an elevated inversion layer at 00 LDT and 08 LDT. As the sun rose, large surface sensible heat flux and rapid rise in temperature occurred over the eastern slope of the Rocky Mountains because the incident solar radiation was more direct over the slope than over the plains. By 10 LDT, strong surface heating has eroded completely the near surface inversion over the eastern edge of Alberta and over the mountain slopes. A small elevated inversion can still be discerned over the plains.

b. Underrunning and low-level moisture transport

In response to the pressure falls, surface wind over the plains veered appreciably, particularly from 12 LDT to 14 LDT (18 UTC to 20 UTC). The resultant upslope flow associated with the lower-branch of the mountain-plain circulation began transporting the moist air to higher elevations as early as 12 LDT. At 14 LDT (Fig. 3.10) the erosion of the capping lid is essentially complete. The lines of TCU displayed in an infrared satellite image taken at 15:34 LDT (see Fig. 11 in SY93a) was a result of this underrunning process.

c. Cross sections of anomalous fields

To illustrate more clearly the development of the synoptic high-low doublet and the mountain-plain circulation, we display cross sections of anomalous fields. If S is a scalar field, the anomaly field (S_A) is defined as

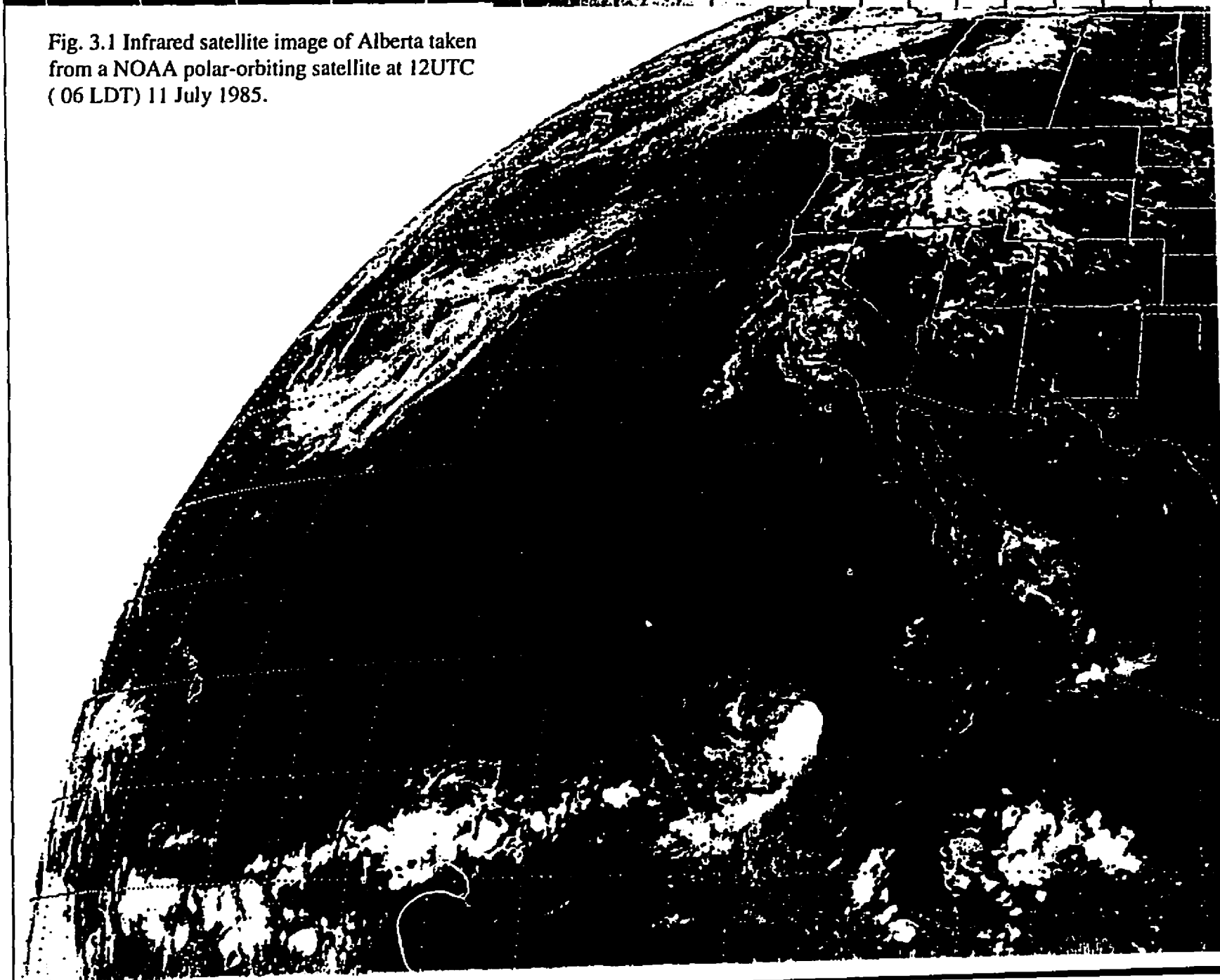
$$S_A - S - [S]$$

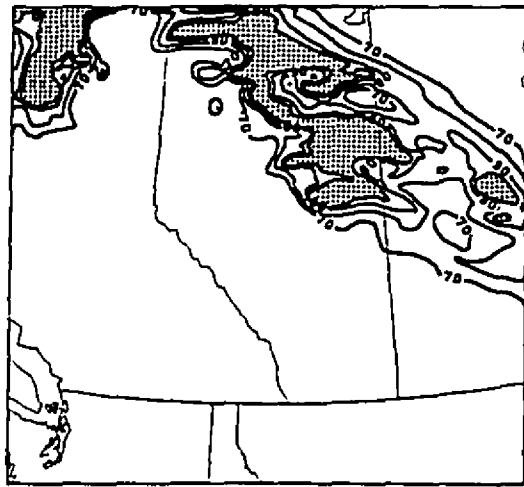
where [S] is the time-averaged field for the period from 08 LDT to 16 LDT.

Fig. 3.11 shows the anomalous mean sea level pressure at 8 LDT, 12 LDT, 18 LDT (14 UTC, 18 UTC, 24 UTC). It is evident that the trough deepened over southeastern Saskatchewan with time and the high ridge was extending into southwestern Saskatchewan. Note also the pressure fall along the foothills at 12 LDT and 18 LDT. Vertical cross sections of the anomalous equivalent potential temperature (θ_e) and anomalous u-component of the wind from LMW (Limestone Mountain) to AQF (Red Deer) are plotted in Fig. 3.12 (The location of vertical cross section refers Fig. 4 in SY93a). The upslope transport of anomalously high θ_e air beneath the capping lid is well illustrated in the 12 and 16 LDT cross sections where high θ_e air from the moist, capped boundary layer is transported by anomalous easterly winds to the narrow band of deepening convection over LMW. Upward transport of low-level easterly momentum by the ascending branch of the solenoidal circulation over the foothills is made evident by the negative anomalous above LMW at 16 LDT (compare with Fig. 15 in SY93a).

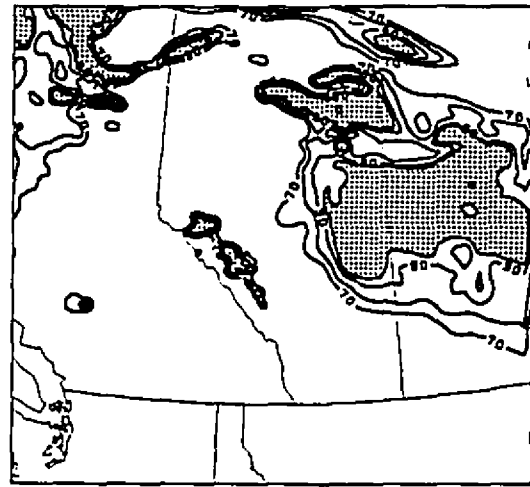
1201 11JL85 38E-4ZA 00561 10681 UC5

Fig. 3.1 Infrared satellite image of Alberta taken from a NOAA polar-orbiting satellite at 12UTC (06 LDT) 11 July 1985.

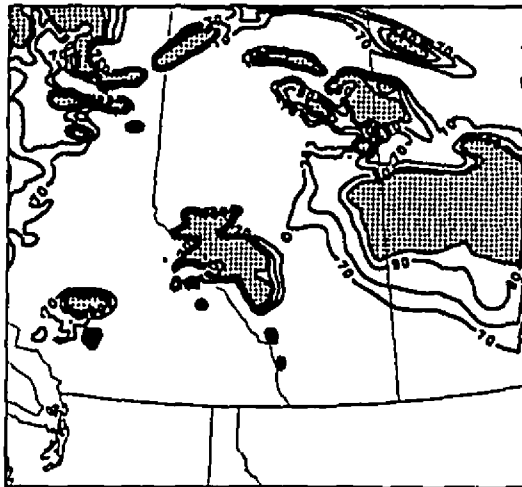




a



b



c

Fig. 3.2 Model predicted relative humidity field at 600mb at a) 06 LDT(12 UTC), b) 14 LDT(20 UTC), and c) 16 LDT(22 UTC) from 10 km control run. Contours are 70%,80%, 90%, and 95%. Shaded areas are relative humidity higher than 95%.

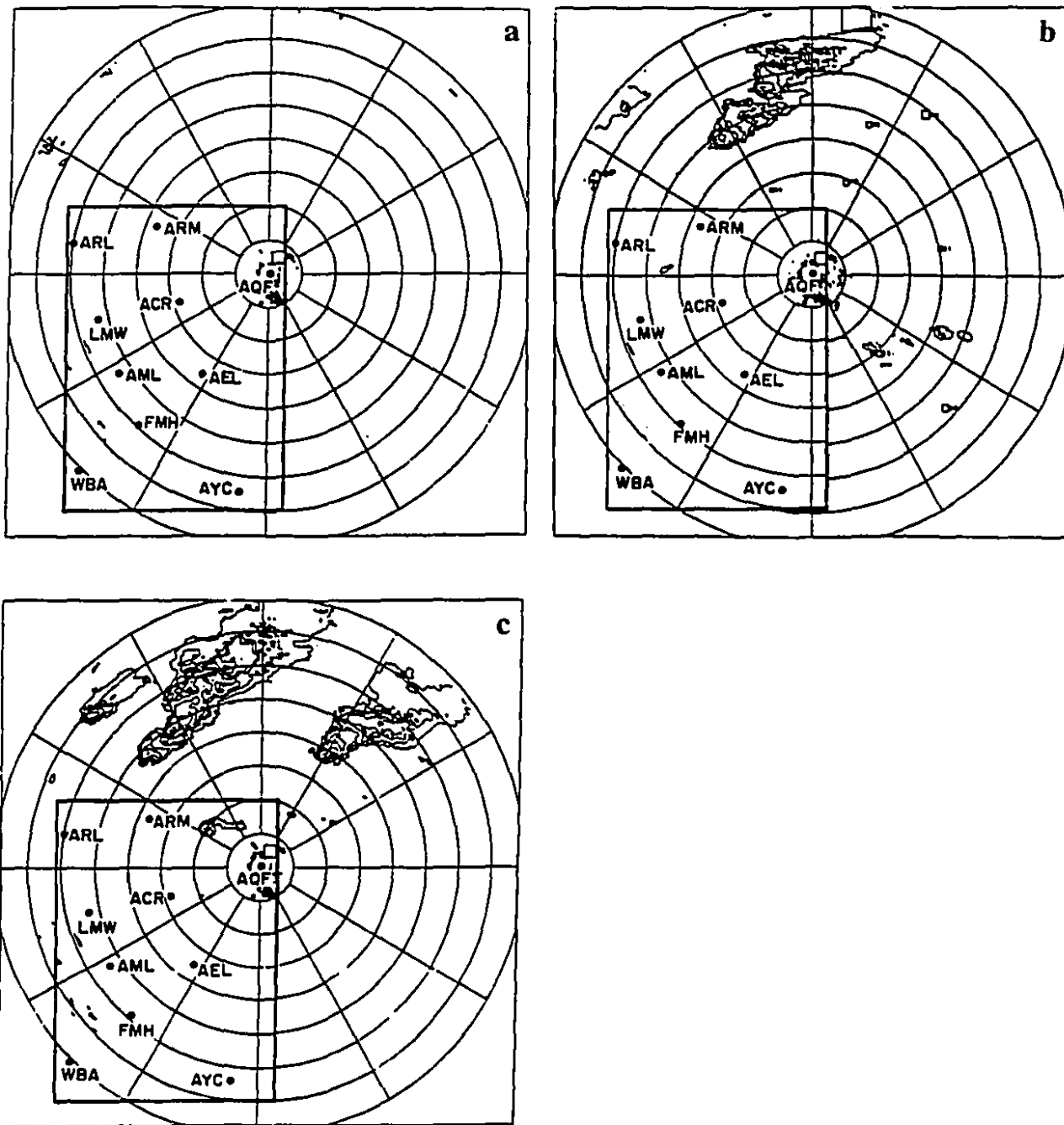


Fig. 3.3 Radar PPIs for a) 16LDT, 11 July (22 UTC, 11 July), b) 18LDT, 11 July (24 UTC, 11 July), and c) 20LDT, 11 July (02 UTC, 12 July) with mesoscale analysis domain included. Range markers are spaced 20 km apart. Contours are of radar reflectivity with an interval of 10 dB. Minimum contour is 20 dBZ. Elevation angle is 1.8°. The weak ground echoes near 240°, at a range of 120 - 140 km, are from the higher peaks in the Alberta foothills.

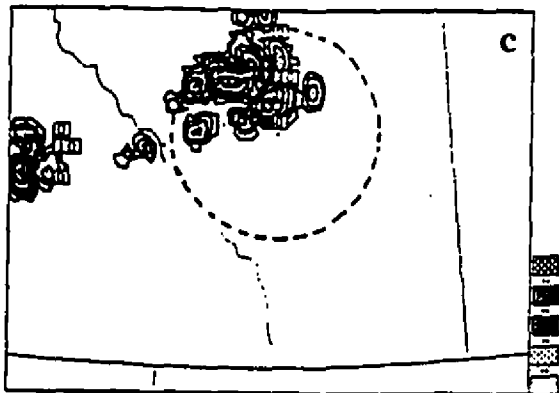
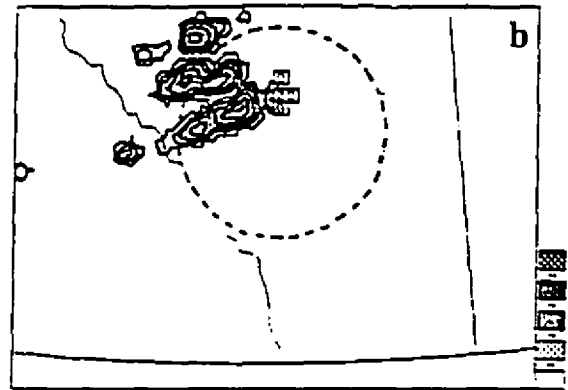
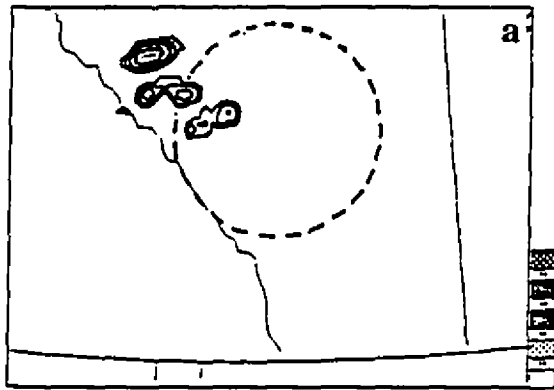


Fig. 3.4 Model predicted radar reflectivity field at 600mb at a) 16 LDT, 11 July 1985 (22UTC, 11 July 1985), b) 18 LDT, 11 July 1985 (00UTC, 12 July 1985), and 20 LDT, 11 July 1985 (02UTC, 12 July 1985) from 10 km control run. Contour interval every 10 dBZ. Minimum contour is 20 dBZ. The dashed circle denotes the 120 km range marker centred at Red Deer.

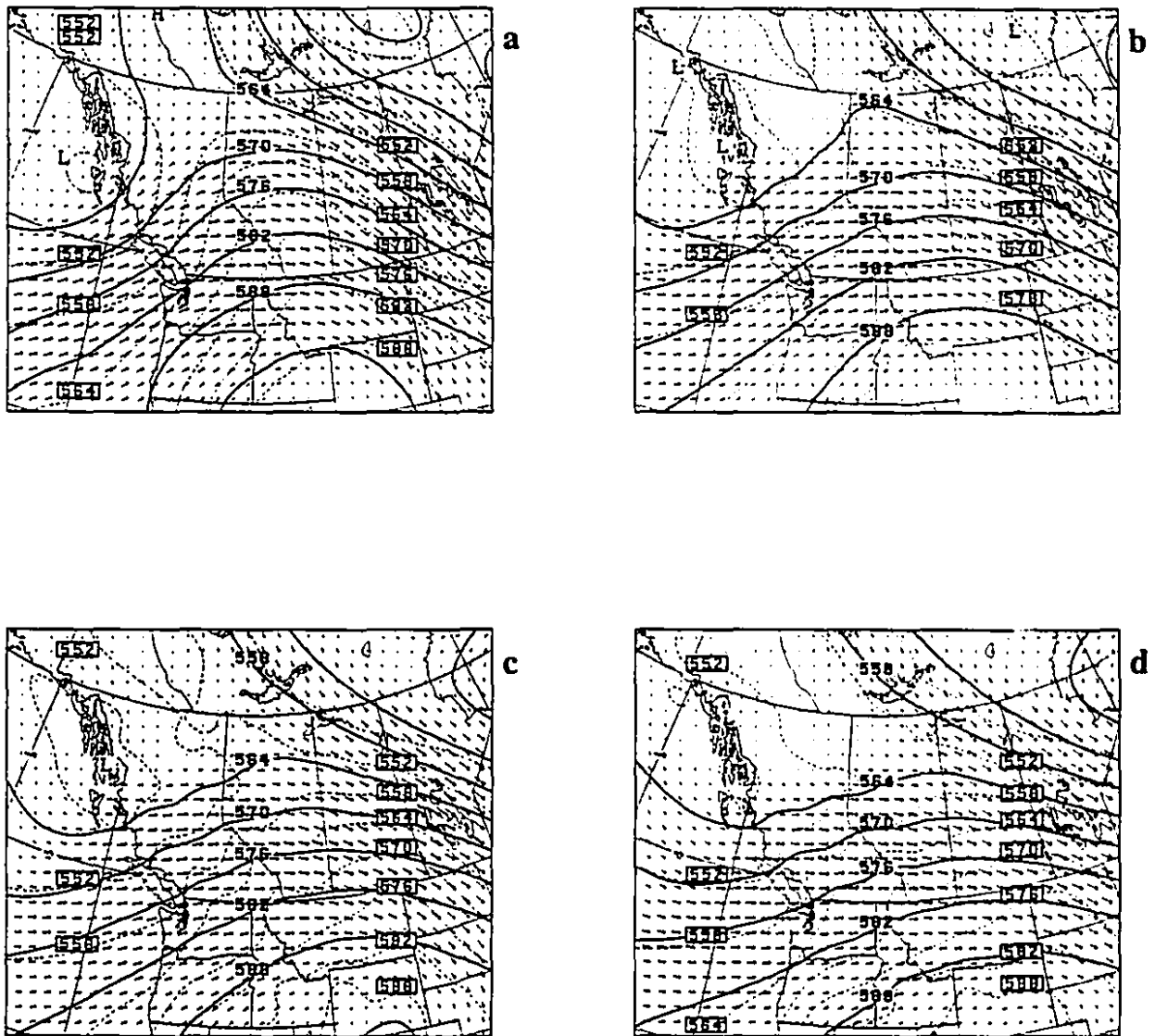


Fig. 3.5 Forecast at 500mb valid at a) Model initial time (18 LDT, 10 July 1985), b) 06 LDT (12 UTC), c) 12 LDT (18 UTC), and d) 18 LDT (24 UTC), 11 July 1985 from 100 km control run. Height (solid), 500-1000mb thickness (dashed) contours are in decameters.

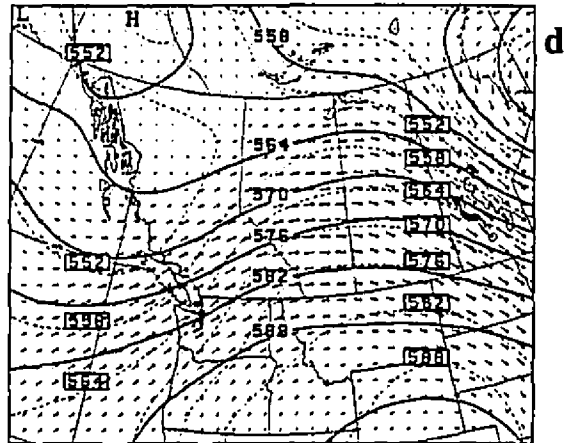
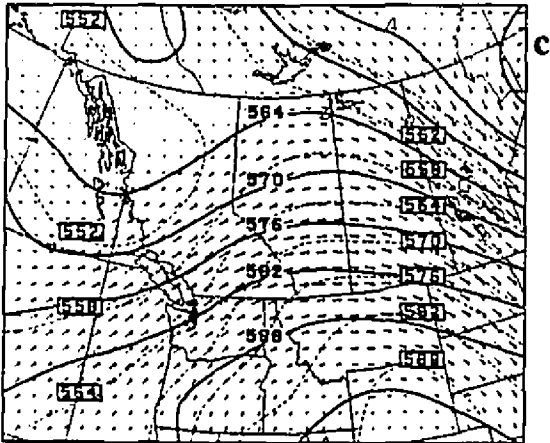
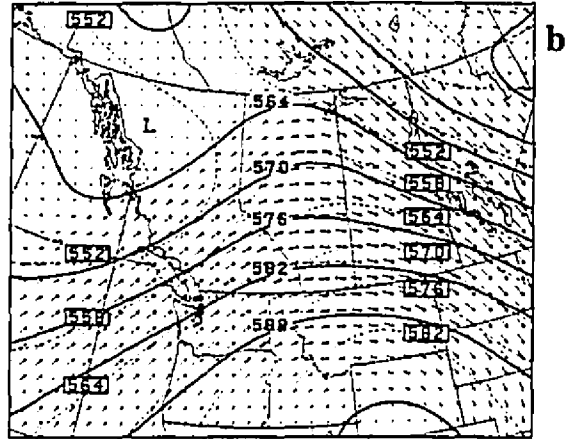
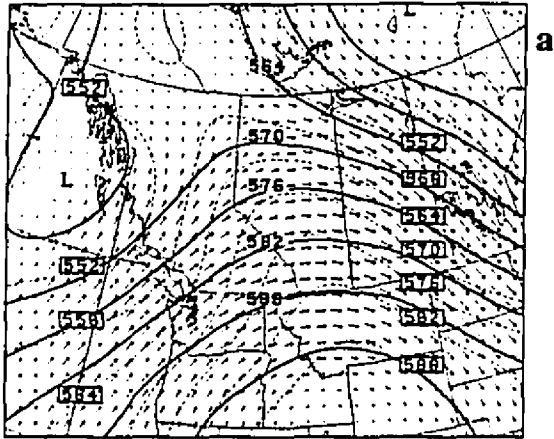
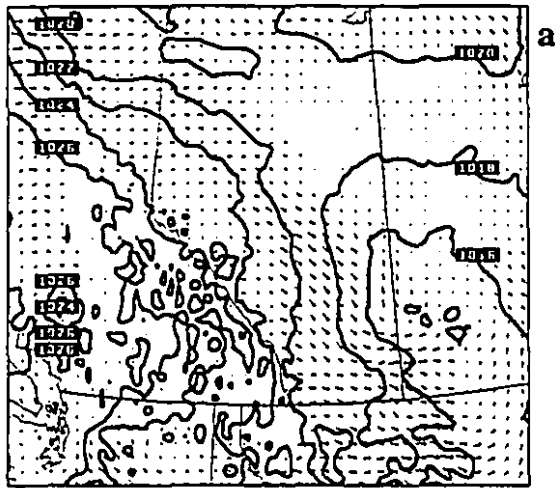
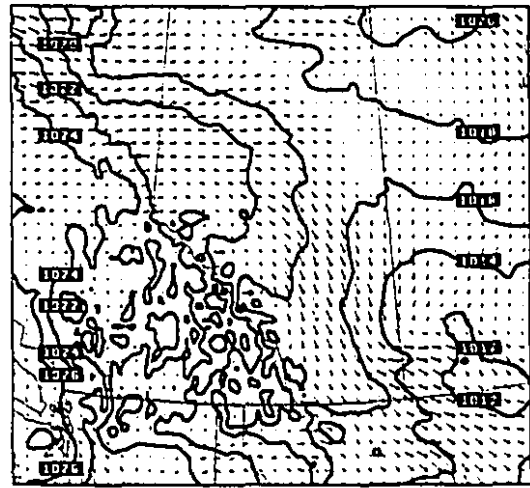


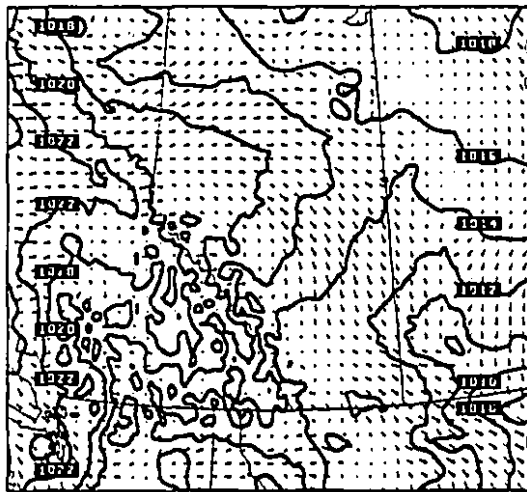
Fig. 3.6 CMC 500mb analysis at a) 18 LDT, 10 July 1985 (00 UTC, 11 July 1985), b) 06 LDT (12 UTC), c) 12 LDT (18 UTC), and d) 18 LDT (24 UTC), 11 July 1985 from 100 km control run. Height (solid), 500-1000mb thickness (dashed) contours are in decameters.



a



b



c

Fig. 3.7 Model predicted MSL pressure and surface wind at a) 08 LDT (14 UTC), b) 12 LDT (18 UTC), and c) 18 LDT (24 UTC), 11 July 1985 from 10 km resolution control run. Contour interval is 2 mb. The largest wind vector is 8m/s.

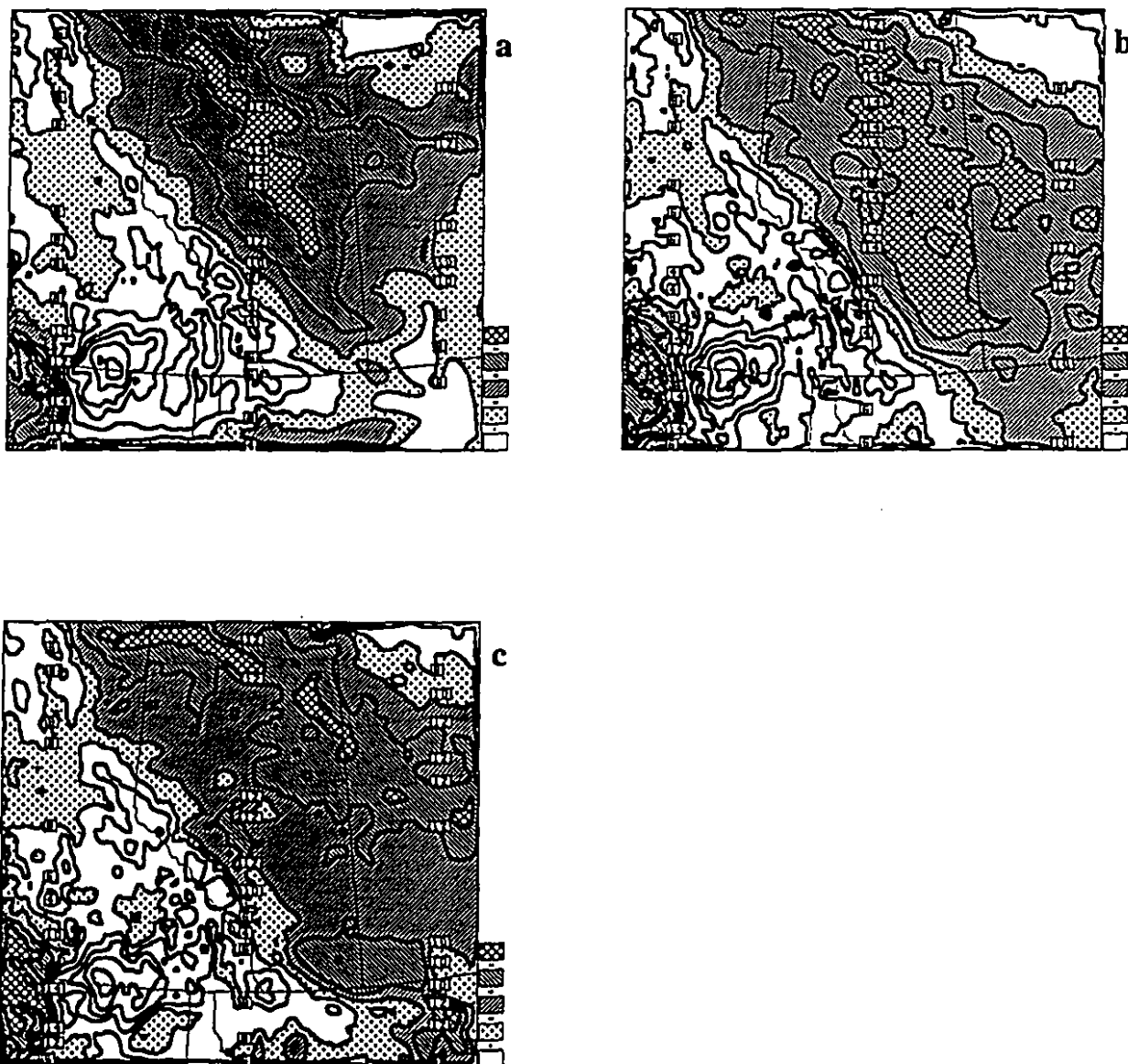


Fig. 3.8 Forecast 10 km resolution surface dew point temperature at a) 08 LDT (14 UTC), b) 12 LDT (18 UTC), and c) 18 LDT (24 UTC), 11 July 1985. Contour interval every 2°C.

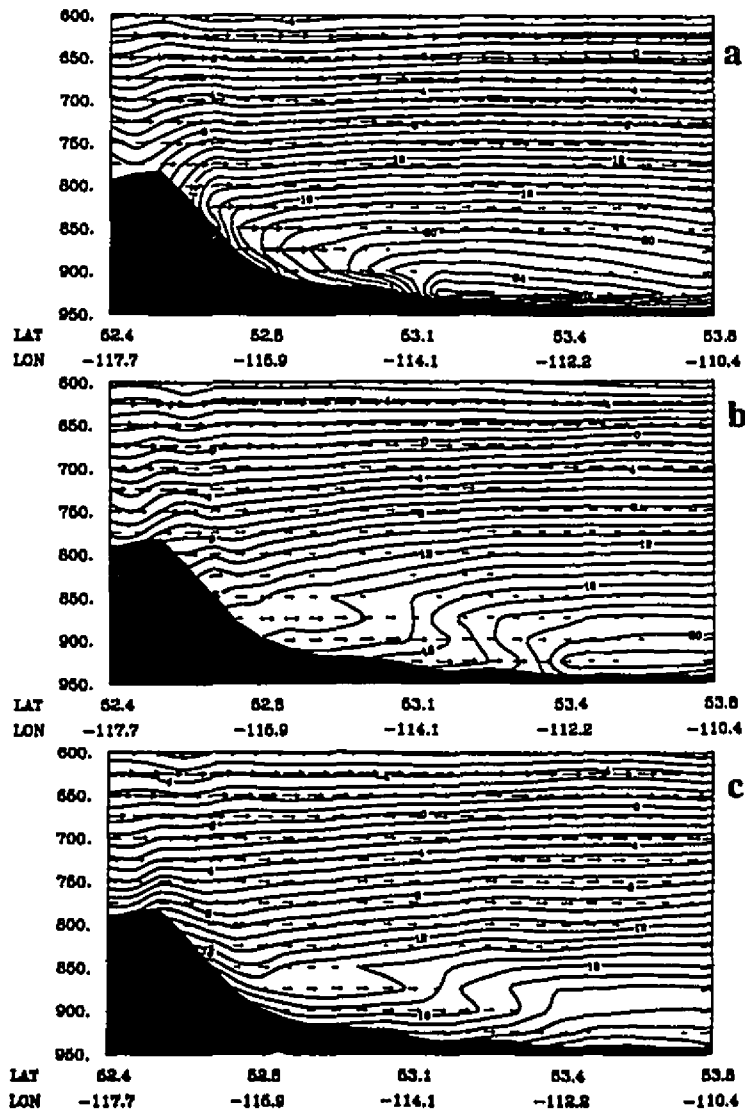


Fig. 3.9 Vertical cross-section of temperature at a) 00 LDT (06 UTC), b) 08 LDT (14 UTC), and c) 10 LDT (16 UTC), 11 July 1985 from 10 km resolution control run. The location of the section is indicated by the line from 1 to 2 in Fig. 2.1. Contour interval is 1°C. The largest wind vector is 13m/s.

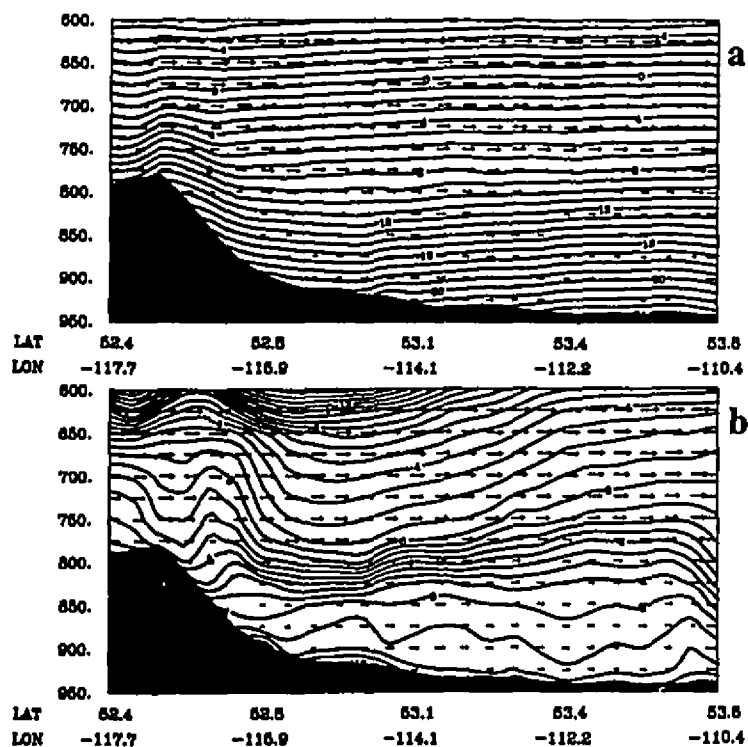


Fig. 3.10 Vertical cross-section of a) air temperature and b) dew point temperature at 14 LDT (20 UTC), 11 July 1985 from 10 km resolution control run. The location of the section is indicated by the line from 1 to 2 in Fig. 2.1. Contour interval is 1°C. The largest wind vector is 13m/s.

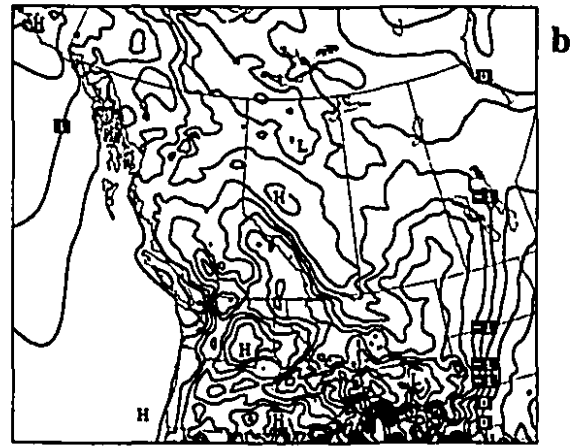
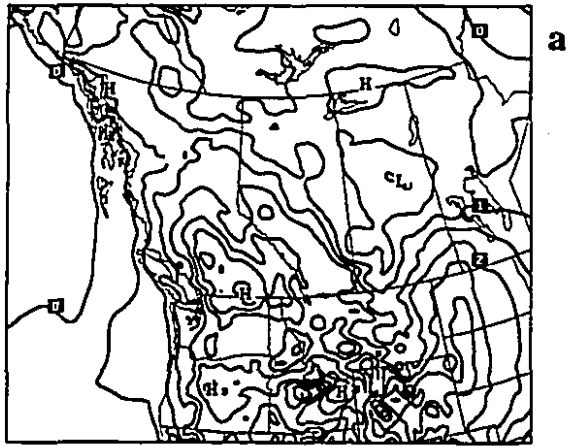


Fig. 3.11 Forecast horizontal section of anomalous mean sea level pressure at a) 08 LDT (14 UTC), b) 12 LDT (18 UTC), and c) 18 LDT (24 UTC) from 25 km resolution run. The contour interval is 0.5 mb.

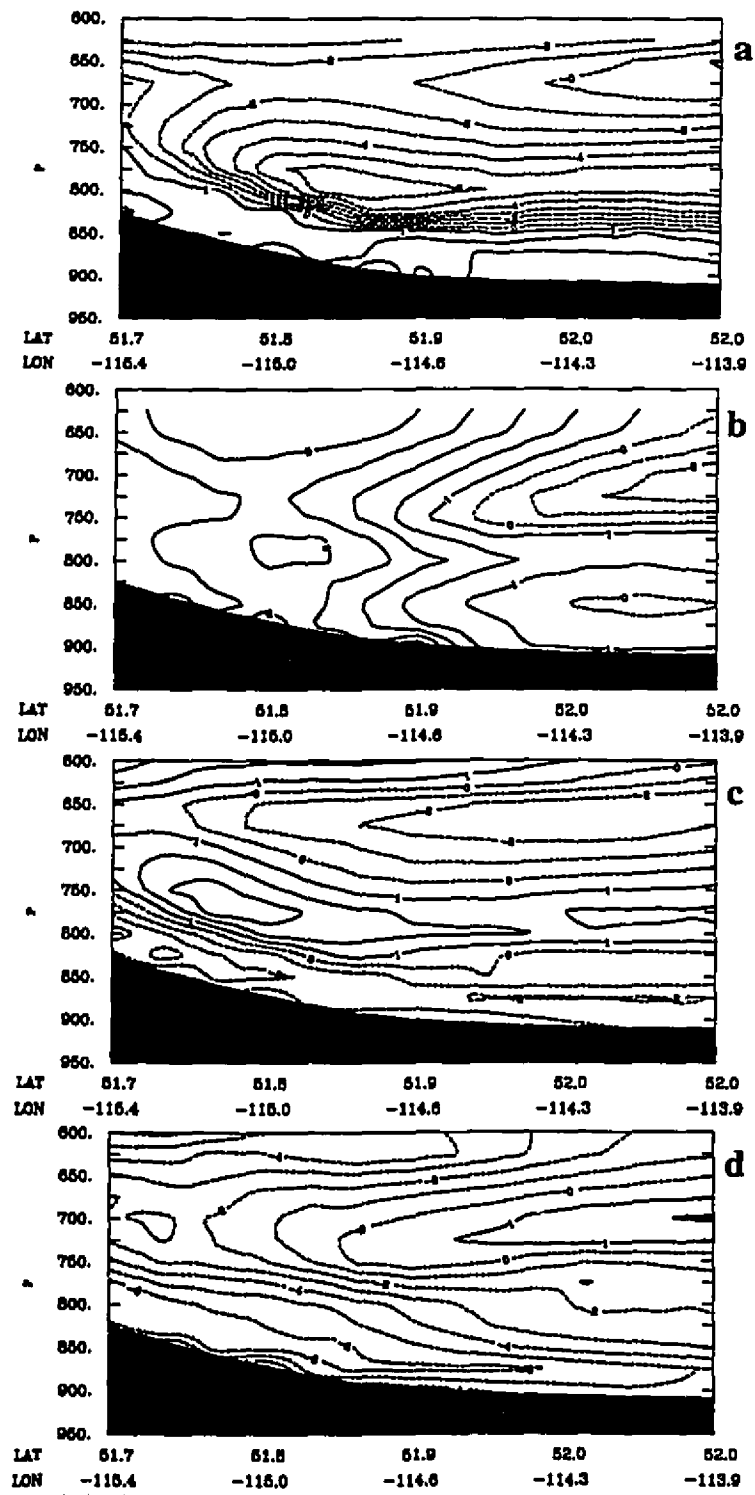


Fig. 3.12 Forecast vertical cross sections of anomalous equivalent potential temperature at a) 12LDT, and b) 16 LDT and anomalous u-component of the wind at c) 12LDT and d) 16 LDT on 11 July 1985 from 10 km resolution run. The contour intervals for temperature and wind are 1°K and 1 ms^{-1} respectively. Dashed contours are negative value. The location of vertical cross section is the same as in Fig. 4 in SY93a.

Chapter 4

Sensitivity Experiments

Having documented the reasonable performance of the model in the control experiment, we proceed to test the importance of various physical processes through a series of sensitivity tests. The experiments NGE, LRT, FLAT, NLW, and NSW were listed in section 2.4. Our discussion will focus on the difference fields obtained by subtracting the relevant fields in the sensitivity runs from the control run. Identical initial and lateral boundary conditions were used in all simulations. All results in this chapter are from the 10 km runs.

1. Expt. NGE- Surface evapotranspiration turned off

In Chapter 3, we pointed out the importance of the moisture tongue in the outbreak of severe convection over the Alberta foothills. A critical question is what is the principle source of this moisture. McKay and Lowe (1960) suggested that an important fraction of the low-level moisture originates from evapotranspiration. Potential sources for evapotranspiration include lakes, marshes, river valleys, foothills forests and irrigated fields. On the other hand, Smith and Yau (SY93b) plotted the climatological (1951-1980) mean maximum daily dew point temperature for July and showed that a tongue of modified maritime tropical air enters the Prairie provinces in southern Manitoba and the tongue extends westward into east-central Alberta. To determine if local evapotranspiration effects are important, Expt. NGE was run

with ground evapotranspiration processes turned off over land surfaces.

Fig. 4.1 display the surface dew point temperature in Expt. NGE at 08 LDT (14 UTC), 12 LDT (18 UTC), and 18 LDT (24 UTC), 11 July 1985. When compared with the results from Expt. CON (Fig. 3.8), it can be seen that the surface dew point temperature in the case with no surface evapotranspiration is, on average, lower by about 5 ~ 6 C°. The southwestward extension of the moisture tongue is conspicuously absent in the sensitivity experiment. To further examine this aspect of the moisture structure, a vertical cross-section was taken approximately along the direction of the surface moisture tongue given in Expt. CON. The section extends from the Rocky Mountains to the Alberta-Saskatchewan border and is delineated by the line running from 1 to 2 in Fig. 2.1. Fig. 4.2 depicts the difference (CON-NGE) field of specific humidity. This field is identically zero at 00 UTC. Six hours later (Fig. 4.2a), very large gradient of the moisture difference appeared. It is of interest to note that the moisture difference was confined below the capping lid (Fig 3.9a) and the isopleths are approximately parallel to the topography. The maximum difference reaches about 4g/kg next to the foothills. Strong gradients in the difference field is found close to the ground and the gradient decreases with height, especially over the foothills region. A similar structure in the isolines is displayed at 14 UTC (08 LDT) (Fig. 4.2b). The maximum moisture difference continued to increase with time near the surface at 10 LDT (Fig. 4.2c), but the gradient of the difference field is reduced in the vertical because of the erosion of the temperature inversion and the development of convection (Fig.3.9b,c). At 12 LDT (Fig. 4.2d) the strong gradients were absent in the difference field as the breakdown of the capping lid and the start of convection transported the moisture upward.

The simulated radar reflectivity field (not shown) in Expt. NGE indicated no radar echo over the foothills during the period of simulation. The absence of severe convection when the environment is deprived of surface evapotranspiration demonstrated that the surface moisture source contributes significantly to the outbreak of severe convection over the province of Alberta.

2. Expts. LRT and FLAT- reduced topographic forcing

SY93a suggested that topography exerts a strong control for the development of convective storms. Topography can induce a mountain-plain circulation and also strengthen the high-low doublet over the lee of the mountains. As a result moisture can be transported into the region of the Alberta foothills. We conducted two sensitivity experiments to examine this suggestion. Expt. LRT was conducted using a 200 km resolution topography. In Expt. FLAT, the topography was completely removed. However, in both runs the distribution of land and ocean are the same as in Expt. CON. It turned out that convective storms failed to appear in the Alberta foothills during the entire integration period in Expt. LRT and Expt. FLAT.

Even with reduced topographical forcing, the upper level features in Expt. LRT and Expt. FLAT were similar to the control. There was a gradual passage of an upstream 500 mb trough and the southeastward displacement with time of the 500-1000 mb thickness pattern from July 11-12.

Figs. 4.3 and 4.4 depict the MSL pressure for the two sensitivity experiments. The pattern is still dominated by a trough of low pressure over southeastern Alberta and a ridge

of high pressure toward the west and northwest. However, when compared with the control run in Fig. 3.7, the deepening rates of the trough in the sensitivity runs were weaker. The surface dew point field for Expt. LRT (Fig 4.5) did not indicate a strong transport of moisture toward the foothill region.

Fig. 4.6 depicts the vertical cross section of the difference in the u-component of the wind between Expt. CON and Expt. FLAT. Large differences in the downslope winds can be noted at 08 and 10 LDT (Fig.4.6a,b). By 12 LDT (Fig. 4.6c), the low level upslope flow below 799 mb and the westerly flow above that level were stronger in the control run. The same observation regarding the u component of the wind can be noted in the difference field between Expt. CON and Expt. LRT (not shown). However, the differences were of a smaller magnitude.

Fig. 4.7 shows the vertical cross section of the specific humidity difference for Expt. CON and Expt. FLAT. A maximum can be found over the plains at 08LDT (Fig. 4.7a). As the sun rises, this region of large difference in moisture extended westward toward the foothills when the mountain-plain circulation started to develop (Fig. 4.7b,c,d).

3. Expts. NLW and NSW - reducing radiative forcing

The formation and the erosion of the capping lid can be affected by longwave cooling and shortwave heating. After sunset, longwave cooling contributes to the formation of the lid. On the other hand, strong surface heating weakens and erodes the inversion layer as the sun rises.

Fig. 4.8 shows the vertical cross-section of temperature in Expt. NLW from 00 LDT to 08 LDT. When compared with Fig. 3.6 of the control, it is evident that the inversion layer did not form during the night time over the plains. Over the foothills, however, the strong downslope flow which developed created an elevated inversion layer which was gradually advected over the western part of the plains when the downslope flow intensified.

Solar heating acts differently from longwave cooling. In principle, the incident solar flux is more direct over the mountain slope than over the plain during the early morning hours. This leads to a rapid rise in the temperature of the slope and a large sensible heat flux from the surface to the boundary layer. Since the boundary layer is generally shallower over elevated terrain, a large sensible heat flux could easily erode most types of temperature inversion which acts to impede free convection. This effect is well demonstrated in the vertical cross-section of temperature from 06 LDT (12 UTC) to 18 LDT (24 UTC), 11 July 1985 in Expt. NSW (Fig. 4.9). It shows clearly that unlike the control experiment, the inversion was not eroded over the slopes and the plains from sunrise to the end of the model integration. No outbreak of convection occurs over the regions of the foothills in this case.

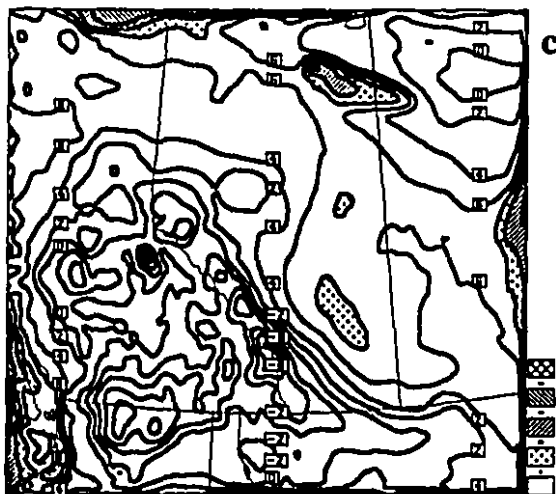
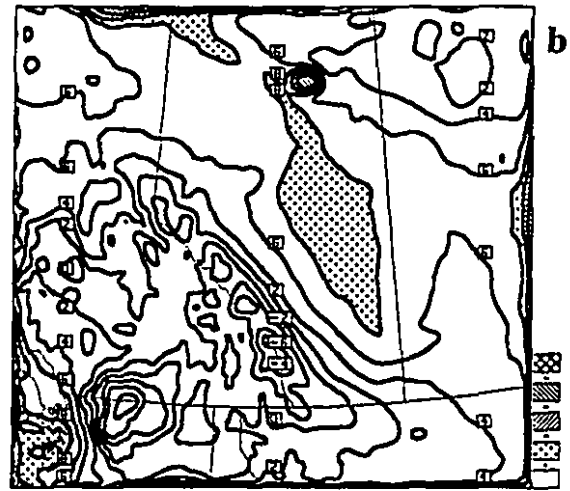
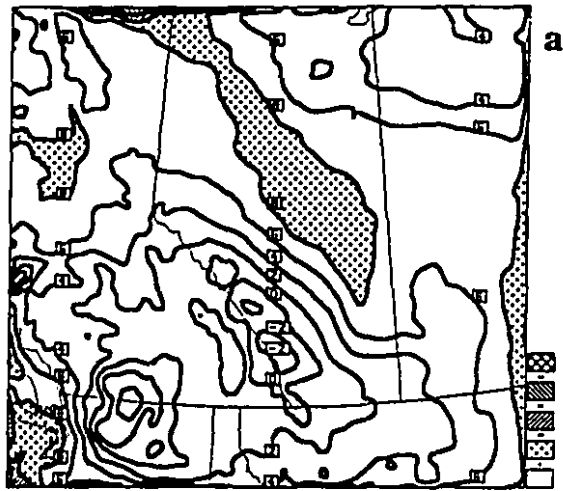


Fig. 4.1 Forecast surface dew point temperature without surface evapotranspiration at a) 08 LDT (14 UTC), b) 12 LDT (18 UTC), and c) 18 LDT (24 UTC), 11 July 1985 from 10 km run. Contour interval is 2°C.

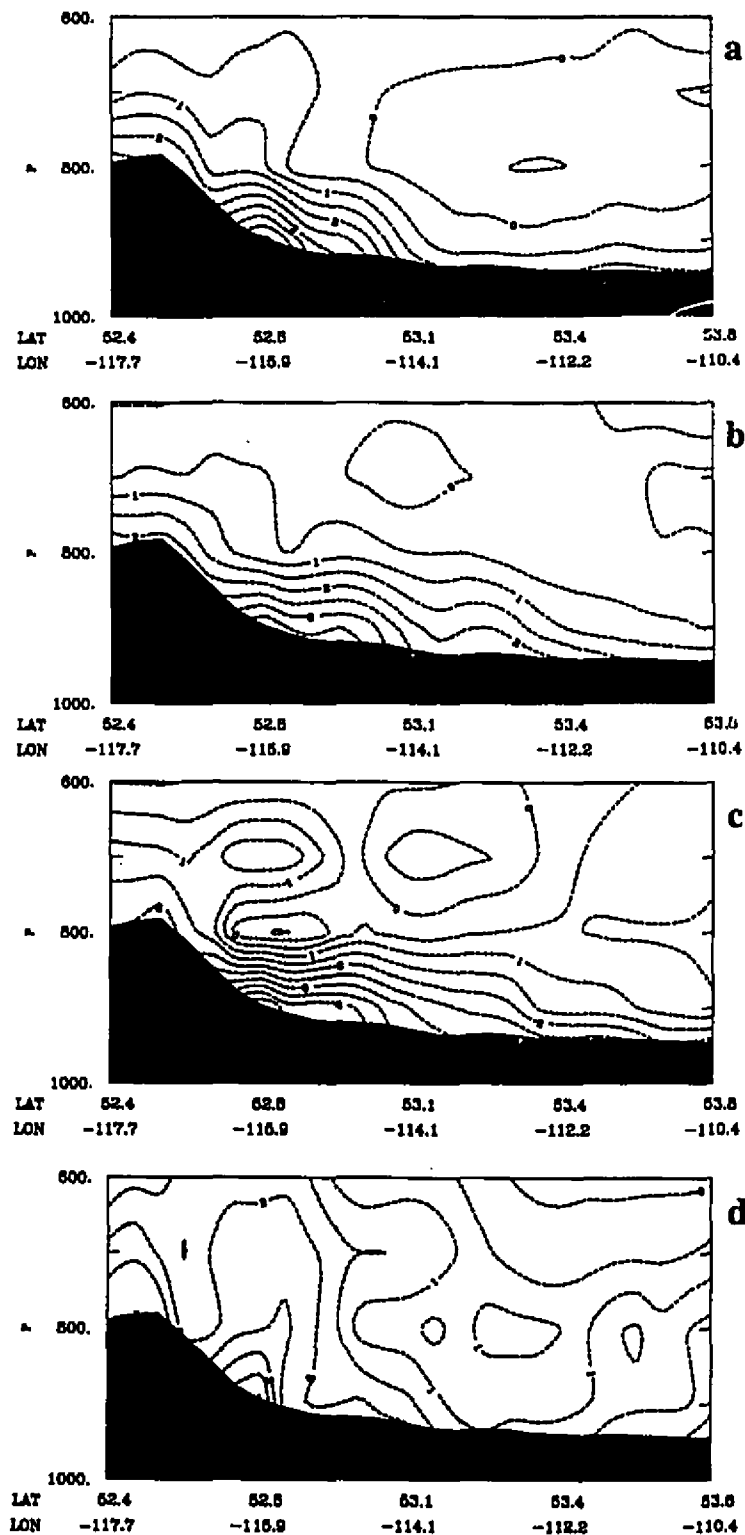


Fig. 4.2 Vertical cross-section of specific humidity difference between Expt. CON. and Expt. NGE at a) 00 LDT (06 UTC), b) 08 LDT (14 UTC), c) 10 LDT (16 UTC), and d) 16 LDT (22 UTC), 11 July 1985. The contour interval is 1 g kg⁻¹. The location of the section is indicated by the line from 1 to 2 in Fig. 2.1.

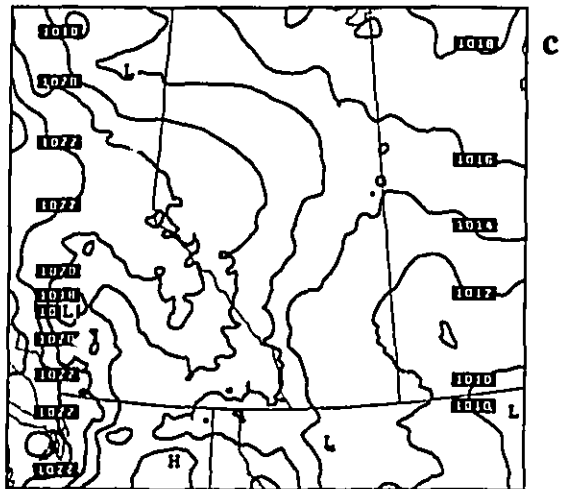
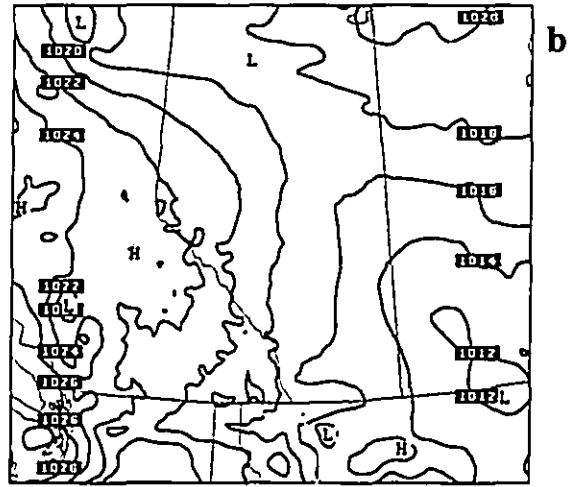
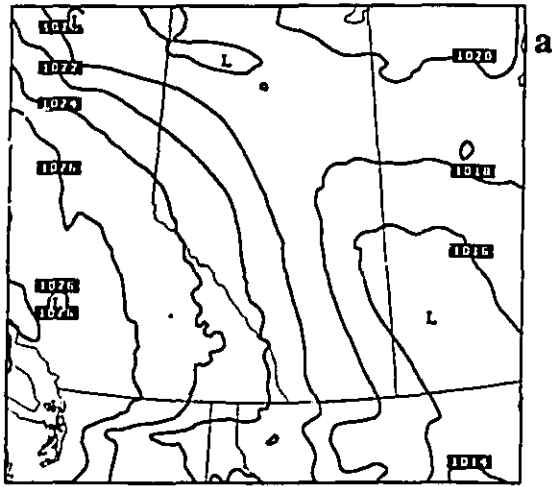


Fig. 4.3 Forecast MSL pressure for Expt. LRT at a) 08 LDT (14 UTC), b) 12 LDT (18 UTC), and c) 18 LDT (24 UTC), 11 July 1985 from 10 km run. The contour interval is 2 mb.

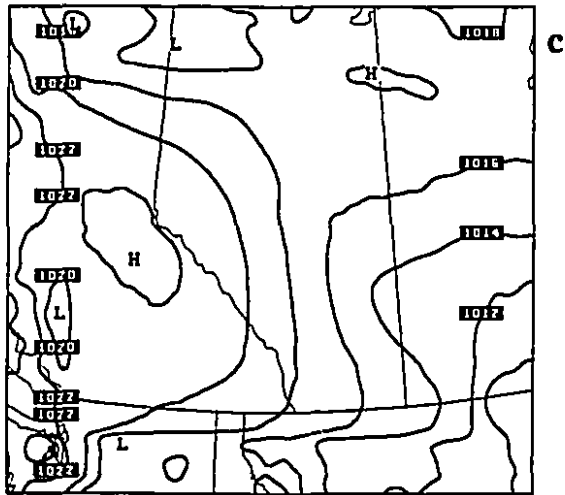
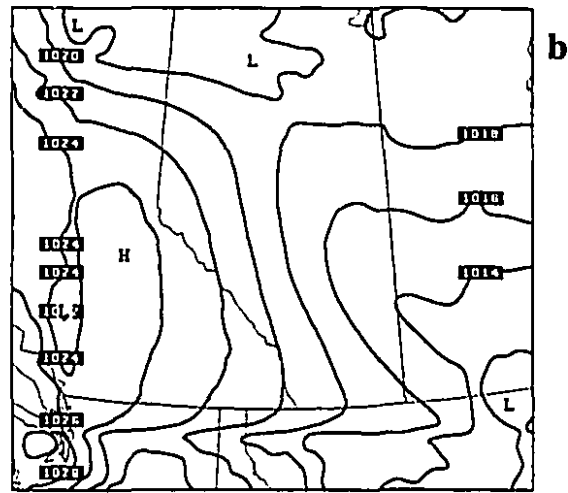
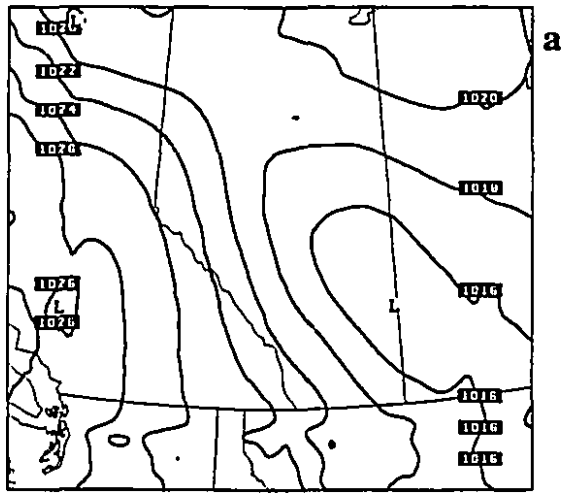


Fig. 4.4 Forecast MSL pressure for Expt. FLAT at a) 08 LDT (14 UTC), b) 12 LDT (18 UTC), and c) 18 LDT (24 UTC), 11 July 1985 from 10 km run. The contour interval is 2 mb.

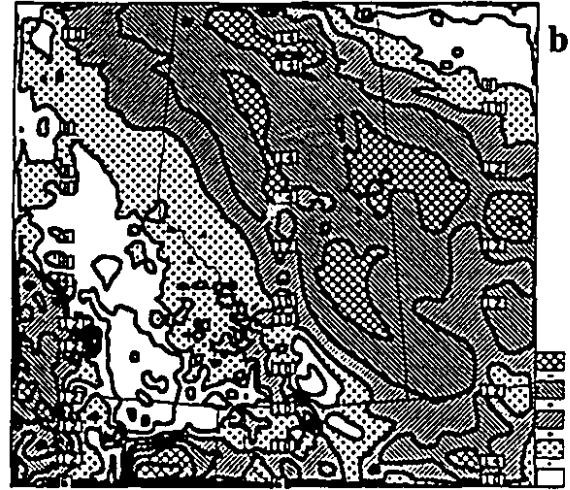
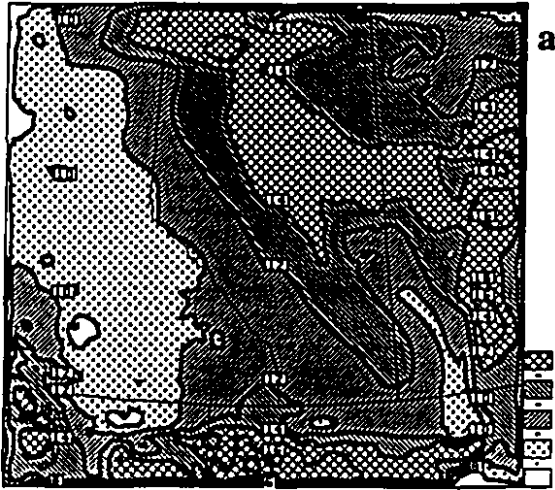


Fig. 4.5 Forecast surface dew point temperature for Expt. LRT at a) 08 LDT (14 UTC), b) 12 LDT (18 UTC), and c) 18 LDT (24 UTC), 11 July 1985 from 10 km run. The contour interval is 2°C.

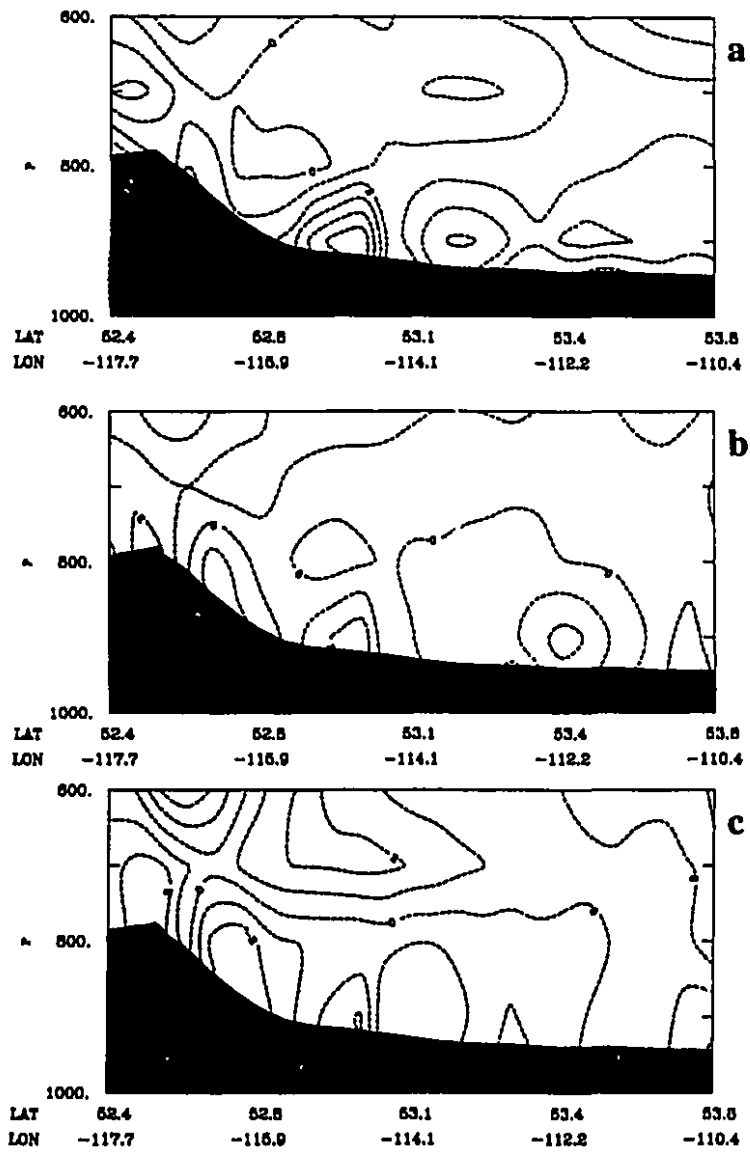


Fig. 4.6 Vertical cross-section of U component of the wind difference between Expt. CON and Expt. LRT at a) 08 LDT (14 UTC), b) 12 LDT (18 UTC), and c) 16 LDT (22 UTC), 11 July 1985. The contour interval is 1 ms⁻¹. The location of the section is indicated by the line from 1 to 2 in Fig. 2.1.

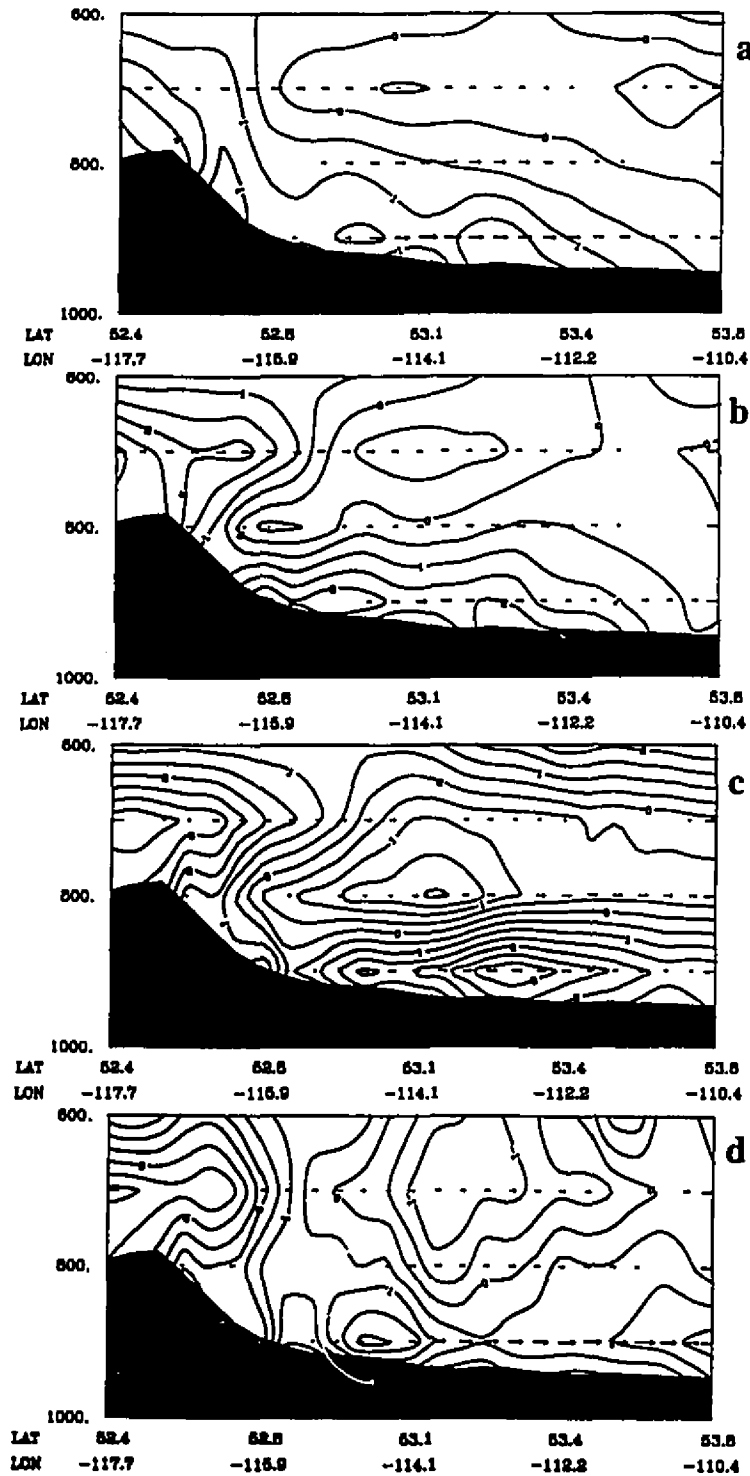


Fig. 4.7 Vertical cross-section of specific humidity difference between Expt. CON and Expt. FLAT at a) 08 LDT (14 UTC), b) 10 LDT (16 UTC), c) 12 LDT (18 UTC), and d) 14 LDT (20 UTC), 11 July 1985. The contour interval is 0.5 gkg^{-1} . The location of the section is indicated by the line from 1 to 2 in Fig. 2.1.

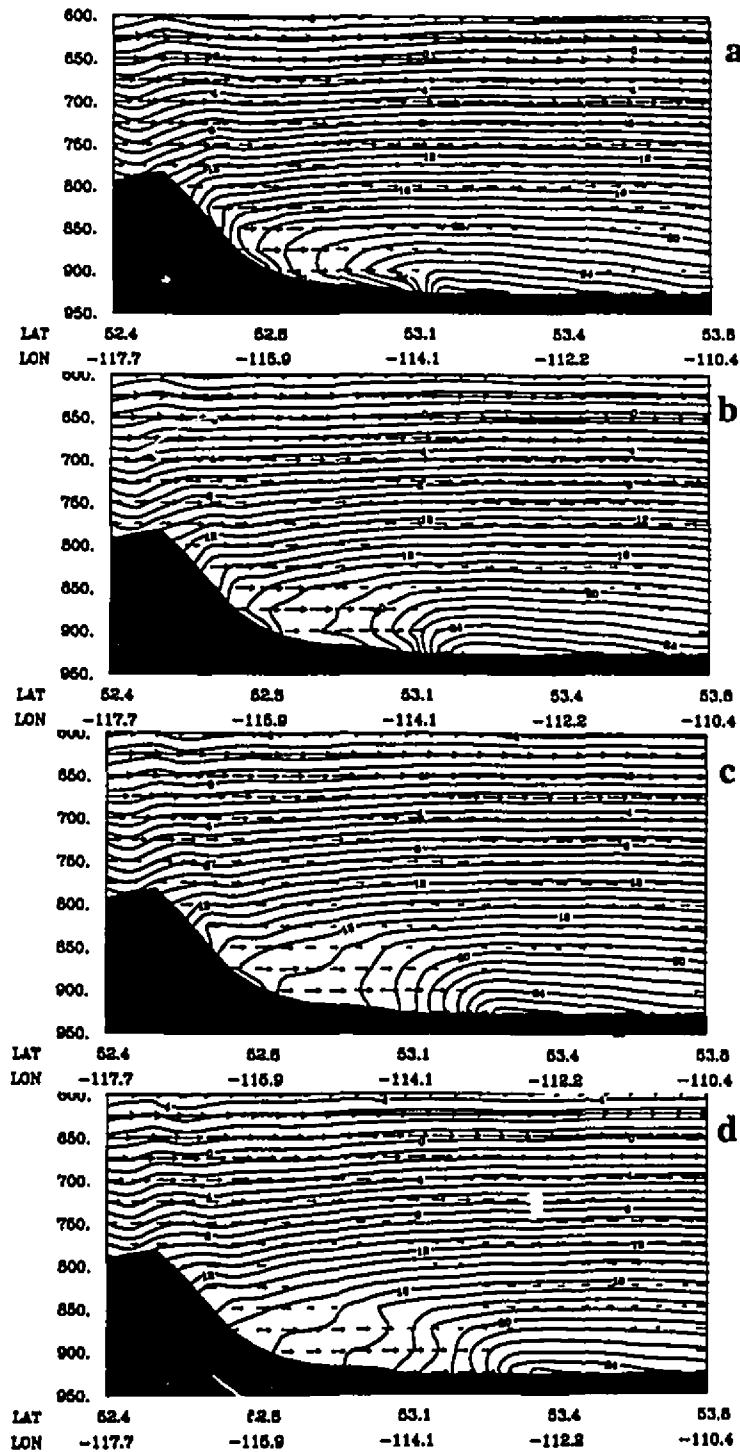


Fig. 4.8 Vertical cross-section of temperature in Expt NLW at a) 00 LDT (06 UTC), b) 02 LDT (08 UTC), c) 04 LDT (10 UTC), and d) 06 LDT (12 UTC), 11 July 1985. The contour interval is 1°C. The largest wind vector is 13ms⁻¹. The location of the section is indicated by the line from 1 to 2 in Fig. 2.1.

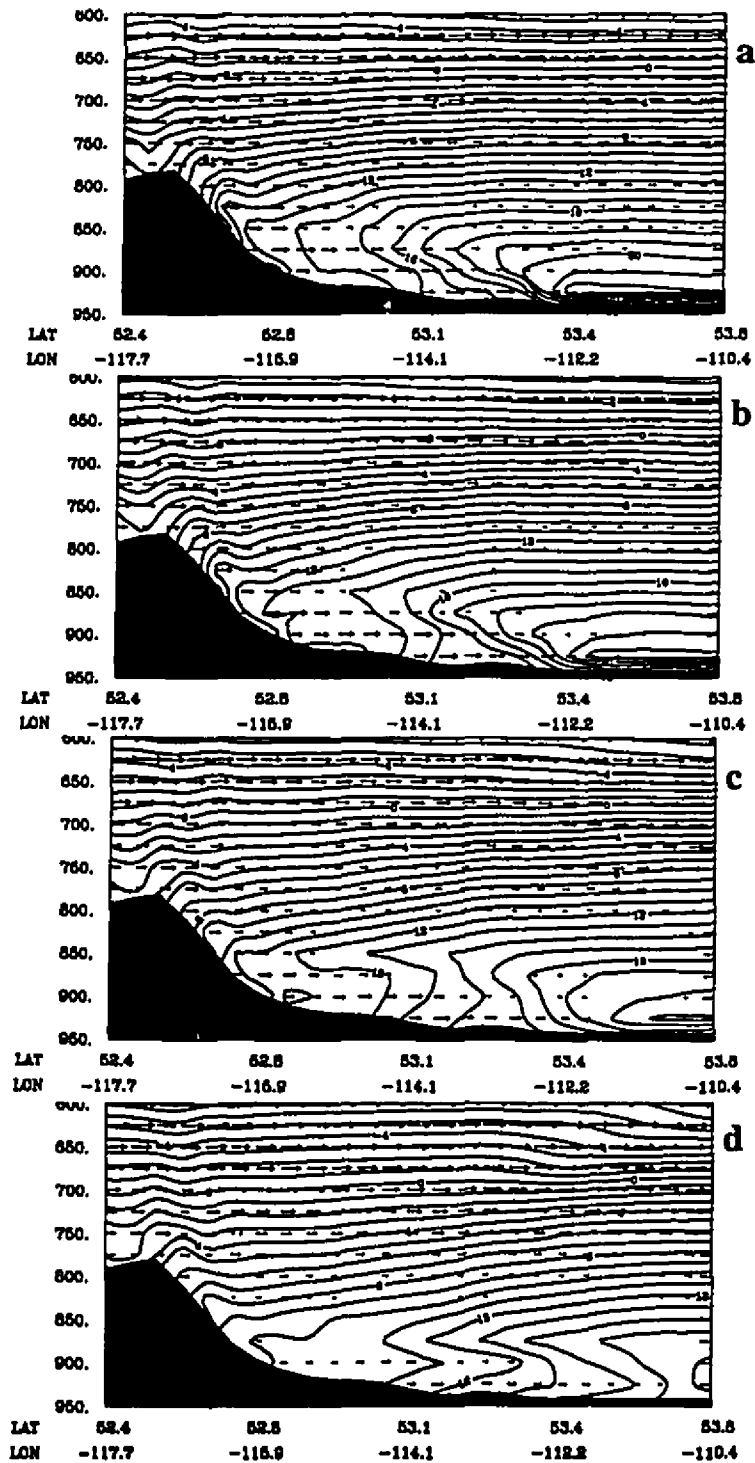


Fig. 4.9 Vertical cross-section of temperature in Expt NSW at a) 06 LDT (12 UTC), b) 08 LDT (14 UTC), c) 12 LDT (18 UTC), and d) 18 LDT (24 UTC), 11 July 1985. The contour interval is 1°C. The largest wind vector is 13ms⁻¹. The location of the section is indicated by the line from 1 to 2 in Fig. 2.1.

Chapter 5

Conclusions

5.1 Summary and conclusions

In this study, an improved version of the mesoscale compressible community model (MC2) has been used to simulate a case of severe convective outbreak on 11 - 12 July 1985. Our objectives are to demonstrate the feasibility of model to forecast properly the outbreak of convection over the Alberta foothills, and to study the effects of surface evapotranspiration, topography, shortwave heating, and long wave radiative cooling through a series of sensitivity experiments. The results of our control experiment confirm the conclusion of Smith and Yau (1993a,b) that

- a). Cumulus convection begins over the Alberta foothills, where the capping lid is quickly eroded by strong surface heating under generally clear sky conditions in the morning.
- b) Severe convective outbreaks would appear to occur when cooling aloft, associated with an approaching synoptic-scale, upper-level trough is in phase with strong surface heating over the foothills. The surface synoptic pressure gradient provides for northeasterly winds over the plains which transport moist plains air towards the foothills and into the lower-branch of the mountain-plain circulation. Such a configuration brings about localized, deep destabilization which given rise to an amplified mountain-plain circulation and underrunning of the capping lid.

The results of the sensitivity experiments show that

- a). While increasing horizontal resolution of mesoscale models will likely improve the timing and location of the severe convective outbreak, the improvement in mesoscale forecast cannot be achieved by simply reducing the grid size. Realistic treatments of terrain, surface processes, and model physics are essential to predict severe convective outbreak.
- b). Local surface evapotranspiration was shown to be an important source of moisture for severe convective outbreak. Without this source of moisture, not enough moisture is available for transport to the foothills regions to feed the convection. As a result, the mountain-plain circulation became ineffective in initiating severe convection.
- c). An often observed condition for severe convection, the presence of a strong capping lid, was found to be formed from two processes. One factor is the presence of radiative cooling at the surface. Another factor is the advection from the downslope flow and the accompanying diabatic warming. Strong surface heating is essential in eroding the lid over the foothills.

5.2 Suggestions for future research

Our numerical simulation and sensitivity tests for severe convective outbreaks represent a significant steps towards understanding how the mesoscale and synoptic-scale processes interact to initiate severe convection over Alberta. It also provides an excellent dataset to compare with the observational analysis.

There are several outstanding questions regarding numerical simulation which are beyond the scope of this dissertation. The foremost is the initial conditions for the simulation.

The initial analysis for the 100km run is interpolated from the standard Global Canadian Meteorological Centre (CMC) analysis. Special observations from the LIMEX dataset have not be used in the model initialization procedure. Incorporation of the mesoscale observations in the initial conditions is highly desirable. Secondly, a 10 km resolution may not be sufficient to simulate the effect of the topography. The study by McQueen (1995), on the influence of grid size and terrain resolution on wind field prediction over east part of U. S. A., indicated that to properly resolve the observed mountain slope wind, a horizontal grid size of 2.5 km together with high terrain and vertical grid resolutions were required. We should explore such possibility in the future.

References

- Al-Jumily, K.J., R.B. Charlton and R.G. Humphries, 1991: Identification of rain and hail with circular polarization radar. *J. Appl. Meteorol.*, **30**, 1075-1087.
- Anthes, R. A., 1977: A cumulus parameterization scheme utilizing a one-dimensional cloud model. *Mon. Wea. Rev.*, **105**, 270-286.
- Benjamin, S. G., and T. N. Carlson, 1986: Some effects of surface heating and topography on the regional severe storm environment. Part I: Three-dimensional simulations. *Mon. Wea. Rev.*, **114**, 307-329.
- Benjamin, S. G., and T. N. Carlson, 1986: Some effects of surface heating and topography on the regional severe storm environment. Part II: Two-dimensional idealized experiments. *Mon. Wea. Rev.*, **114**, 303-343.
- Benoit, R., J. Cote and J. Mailhot, 1989: Inclusion of a TKE Boundary layer parameterization in the Canadian regional finite-element model. *Mon. Wea. Rev.*, **117**, 1726-1750.
- Bolton, D., 1980: The computation of equivalent potential temperature. *Mon. Wea. Rev.*, **108**, 1046-1053.
- Browning, K. A., 1986: Morphology and classification of middle-latitude thunderstorms. *Thunderstorm Morphology and Dynamics*, 2nd Edition. Univ. of Oklahoma press, 133 - 152.
- Bullas, J. M., and A. F. Wallace, 1988: The Edmonton tornado, July 31, 1987. Preprints 15th conf. on Severe Local Storms, Baltimore, Amer. Meteor. Soc., 437 - 443.
- Carlson, T. N. and F. H. Ludlam, 1968: Conditions for the occurrence of severe local storms. *Tellus*, **20**, 203-226.
- Carlson, T. N., S. G. Benjamin, G. S. Forbes and Y.-F. Li, 1983: Elevated mixed layers in the regional severe storm environment: conceptual model and case studies. *Mon. Wea. Rev.*, **111**, 1453-1473.
- Charlton, R.B. B.M. Kachman, and L. Wojtiw, 1995: Urban hailstorms: a view from Alberta. *Natural Hazards*, **12**, 29-75.
- Cotton, W. R., and M. A. Stephens, 1982: The CSU three-dimensional cloud/mesoscale model -1982. Part II: An ice-phase parameterization. *J. Rech. Atmos.*, **16**, 295-320
- Delage, Y., 1988a: The position of the lowest level in the boundary layer of atmospheric

circulation models. *Atmos.-Ocean*, **26**, 329-340.

Delage, Y., 1988b: A parameterization of the stable atmospheric boundary-layer. *Boundary-Layer Meteorol.*, **43**, 365-381.

Fawbush, W. J., R. C. Miller, and L.G. Starrett, 1951: An empirical method of forecasting tornado development. *Bull. Amer. Meteor. Soc.*, **32**, 1 - 9.

Gal-Chen, T and R. C. J. Somerville, 1975: On the use of a coordinate transformation for the solution of the navier-stokes equations. *J. Comput. Phys.*, **17**, 209-228.

Holt, A.R., P.I. Joe, R. McGuinness, E. Torlaschi, T. Nichols, F. Bergwall, D.A. Holland, 1994: Simultaneous polarization and doppler observations of severe convective storms in central Alberta. *Atmos. Res.*, **33**, 37-56.

Kong, F. Y., 1991: Three-dimensional numerical simulations of hailstorms. Ph.D dissertation of Institute of Atmospheric Physics, Chinese Academy of Sciences, 155pp.

Kong, F. Y., M. Huang, and H. Xu, 1990: Three-dimensional numerical simulations of ice phase microphysics in cumulus clouds. Part I: Model establishment and ice phase processes parameterization. *Chinese J. Atmos. Sci.*, **14**, 437-450.

Kong, F. Y., M. Huang, and H. Xu, 1991: Three-dimensional numerical simulations of ice phase microphysics in cumulus clouds. Part II: Effect of multiplication processes. *Chinese J. Atmos. Sci.*, **15**, 459-470.

Kong, F. Y., and M. K. Yau, 1995: Explicit microphysics scheme in MC2. McGill University internal report, 1-5pp, and 14pp.

Kuo, H. L., 1974: Further studies on the parameterization of the influence of cumulus convection on large-scale flow. *J. Atmos. Sci.*, **31**, 1232-1240.

Mailhot, J. and R. Benoit, 1982: A finite-element model of the atmospheric boundary layer suitable for use with numerical weather prediction models, *J. Atmos. Sci.*, **39**, 2249-2266.

Mailhot, J., and C. Chouinard, 1989: Numerical forecasts of explosive winter storms: Sensitivity experiments with a meso- α scale model. *Mon. Wea. Rev.*, **117**, 1311-1343.

Mailhot, J., 1992: Numerical simulation of air mass transformation over the gulf of Mexico. *J. Appl. Meteorol.*, **31**, 946-963.

McQueen J. T., R. R. Draxler, and G. D. Rolph, 1995: Influence of grid size and terrain resolution on wind field predictions from an operational mesoscale model. *J. Appl. Meteorol.*,

34, 2166 - 2181.

Newton, C.W., 1963: Dynamics of severe convective storms. Amer. Meteor. Soc. Meteorol. Monogr. No. 27, 33 - 58.

Newark, M. J., 1984: Canadian tornadoes, 1950 - 1979. *Atmos. - Ocean*, 22, 343 - 353.

Ninomiya, K., 1971: Mesoscale modification of synoptic situations from thunderstorm development as revealed by ATS III and aerological data. *J. Appl. Meteorol.*, 10, 1103 - 1121.

Orville, H. D., and F. J. Kopp, 1977: Numerical simulation of the life history of a hailstorm. *J. Atmos. Sci.*, 34, 1596-1618.

Reuter, G.W. and N. Aktary, 1995: Convective and symmetric instabilities and their effects on precipitation: Seasonal variations in central Alberta during 1990 and 1991. *Mon. Wea. Rev.*, 123, 153-162.

Smith, S. B., 1990: The Causes of convective outbreaks in Alberta. Ph. D. Dissertation, McGill University, 174pp.

Smith, S. B. and M. K. Yau, 1993: The Causes of severe convective outbreaks in Alberta, Part I: A comparison of a severe outbreak with two non-severe events. *Mon. Wea. Rev.*, 121, 1099-1125.

Smith, S. B. and M. K. Yau, 1993: The causes of severe convective outbreaks in Alberta, Part II: Conceptual model and statistical analysis. *Mon. Wea. Rev.*, 121, 1126-1133.

Strong, G. S., 1986: Synoptic to mesoscale dynamics of severe thunderstorm environments: A diagnostic study with forecasting applications. Ph. D. dissertation, the University of Alberta, 345pp.

Tanguay, M., A. Robert and R. Laprise, 1990: A semi-implicit semi-lagrangian fully compressible regional forecast model. *Mon. Wea. Rev.*, 118, 1970-1980.

Tripoli, G. J. and W. R. Cotton, 1989: Numerical study of an observed orogenic mesoscale convective system. Part I: Simulation genesis and comparison with observation. *Mon. Wea. Rev.*, 117, 273-304.

Tripoli, G. J. and W. R. Cotton, 1989: Numerical study of an observed orogenic mesoscale convective system. Part II: Analysis of governing dynamics. *Mon. Wea. Rev.*, 117, 305-328.

Wojtiw, L., 1975: Climatic summaries of hailfall in Central Alberta (1957 - 73). Alberta Research Council, 102pp.